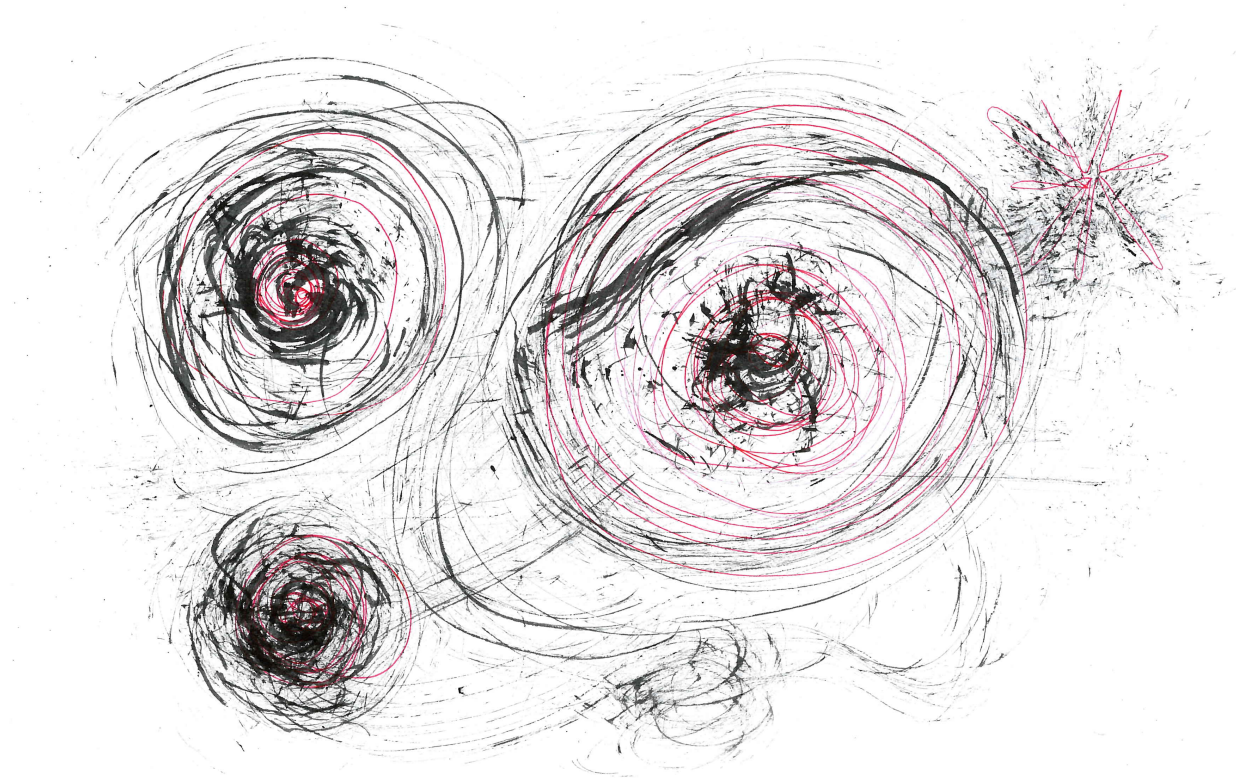




Gas and Dust Distributions in Galactic Red Supergiant Clusters

A Multi-Wavelength Study of RSGC2

Master's Thesis in Physics

EMMA CHAN

DEPARTMENT OF PHYSICS AND ASTRONOMY

CHALMERS UNIVERSITY OF TECHNOLOGY
Gothenburg, Sweden 2026
www.chalmers.se

Master's Thesis 2026

Gas and Dust Distributions in Galactic Red Supergiant Clusters

A Multi-Wavelength Study of RSGC2

EMMA CHAN



CHALMERS
UNIVERSITY OF TECHNOLOGY

Department of Physics and Astronomy
Chalmers University of Technology
Gothenburg, Sweden 2026

Gas and Dust Distributions in Galactic Red Supergiant Clusters
A Multi-Wavelength Study of RSGC2
EMMA CHAN

© EMMA CHAN, 2026.

Supervisor: Mark Siebert, Department of Physics and Astronomy
Co-Supervisor: Elvire De Beck, Department of Physics and Astronomy
Examiner: Elvire De Beck, Department of Physics and Astronomy

Master's Thesis 2026
Department of Physics and Astronomy
Chalmers University of Technology
SE-412 96 Gothenburg
Sweden
Telephone +46 31 772 1000

Cover: An artistic interpretation of three or four Red Supergiants made by my friend Jacob Wästvind.

Typeset in LaTeX
Gothenburg, Sweden 2026

Gas and Dust Distributions in Galactic Red Supergiant Clusters
A Multi-Wavelength Study of RSGC2
EMMA CHAN
Department of Physics and Astronomy
Chalmers University of Technology

Abstract

Red Supergiant (RSG) stars are among the most massive and luminous stars in the universe, and studying their environments offers unique insights into stellar evolution and the interstellar medium. This thesis presents a multi-wavelength analysis of the molecular gas and dust surrounding Stephenson 2 (RSGC2), one of the most RSG-rich clusters known in the Milky Way, located in the crowded Scutum-Crux region of the Galaxy. By using large-scale public surveys (GRS, FUGIN, COHRS, GLIMPSE, and Herschel/PACS) and high-resolution ALMA observations, we map the spatial and kinematic structure of the cluster environment across distinct line-of-sight velocity ranges.

The results reveal a complex arrangement of foreground and background Galactic structures, mapping distinct spiral arm crossings in the velocity window of -25 to 115 km/s. Notably, the nearby Sagittarius arm structures align closely with prominent dust emission features. The IRAS source that was previously attributed to a localized bow shock may instead originate from this spiral arm geometry, though its possible association with the cluster velocity cannot be excluded. Moreover, at the cluster velocities ($90 - 115$ km/s), the results show that massive stars within the cluster core have actively cleared their immediate surroundings of molecular gas, consistent with stellar feedback driven gas expulsion. We also identify a dense molecular gas barrier that physically separates the main cluster from a South-West component of the cluster, suggesting a complex or decoupled formation history. Furthermore, several prominent large-scale dust structures are identified and discussed in terms of their possible association with the cluster or foreground spiral arm emission. Together, these results provide new insights into the multi-phase interstellar kinematics as well as gas and dust distributions within RSGC2.

Keywords: Red Supergiants, RSG, RSGC2, Stephenson 2, Gas, Dust, ISM, CO emission

Acknowledgements

Starting this project without knowing where it was going to land was genuinely such a fun and challenging experience. I am more than grateful that I had the opportunity to do this with my supervisors, Mark Siebert and Elvire De Beck, whom have been extremely supportive and helpful during the course of this project. Thank you Mark for always welcoming me to your office whenever I needed and patiently answering all my questions. Thank you Elvire for your encouragement and insights which helped me improve my thesis. Working with both of you has been a definitive highlight and I truly could not have asked for better supervisors.

Furthermore, I would like to thank all the lovely people from the Evolved Stars meetings, Wouter Vlemmings, Theo Khouri, Matthias Maercker, Miora Andriantsaralaza, Behzad Bojnordiarbab and Léa Planquart, who provided me with advice, and made me feel welcome. I also want to thank all the fellow friends who wrote their thesis on the same floor as me. Thank you for all the laughs, coffee breaks and the collective stress we could share. A special thanks to Jacob Wästvind for drawing the coverpage of my thesis.

Lastly, I want to extend my heartfelt gratitude to all friends and family who have always supported me. I am forever grateful to have such great people around me.

Emma Chan, Gothenburg, June 2026

List of Acronyms

Below is the list of acronyms that have been used throughout this thesis listed in alphabetical order:

ALMA	Atacama Large Millimeter/Submillimeter Array
CASA	Common Astronomy Software Application
CO	Carbon Monoxide
COHRS	^{12}CO High-Resolution Survey
DEC	Declination
GLIMPSE	Galactic Legacy Infrared Midplane Survey Extraordinaire
GRS	Galactic Ring Survey
Hi-Gal	Herschel infrared Galactic Plane Survey
HR-Diagram	Hertzsprung-Russell Diagram
ISM	Interstellar medium
LSR	Local Standard of Rest
RA	Right Ascension
RSG	Red Supergiant
RSGC2	Red Supergiant Cluster 2 or Stephenson 2
YMC	Young Massive Cluster

Contents

List of Acronyms ix

1 Introduction 1
- 1.1 Stellar Evolution . . . 1
- 1.2 Red Supergiants . . . 2
- 1.3 Young Massive Star Clusters . . . 3
- 1.4 The Stephenson 2 Cluster . . . 4
- 1.5 Aim and Outline . . . 5

2 Theory 7
- 2.1 Coordinates of our galaxy . . . 7
- 2.2 The Milky Way and Its Spiral Arms . . . 7
- 2.3 Interstellar Medium . . . 8
  - 2.3.1 CO as a tracer . . . 9
  - 2.3.2 Interstellar Dust . . . 10
- 2.4 Radio Astronomy: Radio Telescope and Interferometers . . . 10
- 2.5 Radio Observable Quantities . . . 11
  - 2.5.1 Flux Density and the Jansky . . . 11
  - 2.5.2 Brightness Temperature . . . 11
  - 2.5.3 Antenna temperature . . . 12
  - 2.5.4 Main beam brightness temperature . . . 12

3 Observational Data and Methods 15
- 3.1 Surveys . . . 15
  - 3.1.1 ALMA . . . 16
  - 3.1.2 Galactic Ring Survey . . . 17
  - 3.1.3 FUGIN . . . 17
  - 3.1.4 COHRS . . . 18
  - 3.1.5 GLIMPSE . . . 18
  - 3.1.6 Herschel/PACS . . . 18
- 3.2 Velocity Ranges . . . 18
- 3.3 Spectral Plot . . . 19
  - 3.3.1 Line intensities and ratios . . . 19
  - 3.3.2 Propagation of Uncertainties . . . 20
- 3.4 Channel Maps . . . 20
- 3.5 Moment Maps . . . 21
- 3.6 Dust emission images . . . 21

4 Results 23

4.1 Spectral Analysis . . . 23
4.2 The Galactic Spiral Arms . . . 25
4.2.1 The Sagittarius Arm, IRAS 18364-0605, PACS-A and PACS-B. . . . 26
4.3 At Cluster Velocities . . . 28
4.3.1 The SW barrier and the infrared sources . . . 31
4.4 CO Line Ratios . . . 36

5 Discussion **39**
5.1 The Spiral Arms . . . 39
5.2 The Infrared Sources . . . 40
5.2.1 IRAS 18369-0557 . . . 40
5.2.2 IRAS 18367-0556 . . . 41
5.2.3 PACS-A and PACS-B . . . 41
5.2.4 IRAS 18364-0605 . . . 43
5.2.5 PACS-C and PACS-D . . . 44
5.3 The Molecular Gas Barrier and The South-West Region . . . 45
5.4 CO line Ratios . . . 46
5.5 Future Work . . . 46

6 Conclusion **49**

Bibliography **51**
References . . . 51

A Appendix **I**
A.1 ALMA spectral profile . . . I
A.2 Average Brightness Temperature Over the Spectral Range . . . II
A.3 Moment 0 map of the Outer Arm . . . III
A.4 More Channel maps over the Sagittarius Arm . . . III
A.5 Ratio for all sources . . . IV
A.6 ALMA survey . . . V

1

Introduction

Stars exhibit a wide range of masses and depending on their initial mass, the evolution and stages they go through will differ. One significant driver of stellar evolution is that of mass loss. All stars continuously shed material into their surroundings throughout their lives and the evolution of a star is heavily affected by this phenomenon. The rate and mechanisms behind this mass loss differ depending on the star and its evolutionary stage. High mass-loss rates are found in stars that are hot and luminous, or cool with low surface gravity. Massive stars in particular, eject mass very efficiently through strong stellar winds, creating large-scale dusty circumstellar envelopes. These vigorous outflows affect not only how these stars are observed, but also the properties of the medium surrounding them. More than half of the mass loss that occurs in a massive star's lifetime happens after it has exhausted its core hydrogen and evolved off the main sequence. A substantial fraction of this mass is shed during the Red supergiant (RSG) phase. RSGs represent some of the most efficient dust producing stars that contribute to the surrounding environment through mass loss. Understanding the mechanisms behind RSG mass loss is therefore vital to the broader understanding of galactic chemical evolution and the progenitor conditions of core-collapse supernovae.

1.1 Stellar Evolution

Stellar evolution aims to describe the evolution of stars over time. The life cycle of a star is most clearly illustrated using the *Hertzsprung-Russell* (HR) diagram, which plots stellar luminosity against effective temperature (see Fig. 1.1) [1]. For a majority of a star's lifetime, it resides in an evolutionary phase known as the *main sequence* [1]. On the HR diagram, main sequence stars occupy a distinct diagonal band where they fuse hydrogen in their cores. During this phase, the star remains in a state known as *hydrostatic equilibrium* [1]. This means that the inward pull of gravity is largely balanced by the outward force of gas and radiation pressure. However, stars in this phase can still experience gradual changes such as mass loss. To maintain this balance of hydrostatic equilibrium, it is necessary for the star to have a sharp temperature and density gradient, where the core is hotter and denser than the atmosphere [1]. To sustain the temperature gradient during its long lifetime, the star relies on an internal energy source, nuclear fusion. This process occurs in the center of the star where the conditions are extreme enough for nuclear fusion.

Once the nuclear energy sources are exhausted, the outward pressure drops and the star will begin the last stages of its life [1]. The nature of these late stages of evolution depends heavily on the star's initial mass, which also dictates its trajectory across the HR diagram. In brief, for low-mass stars, the core will compress into a dense, small star known as a white dwarf [1]. For high-mass stars, the core will collapse in a few seconds, triggering a supernova explosion, leaving either a neutron star or a black hole behind [1].

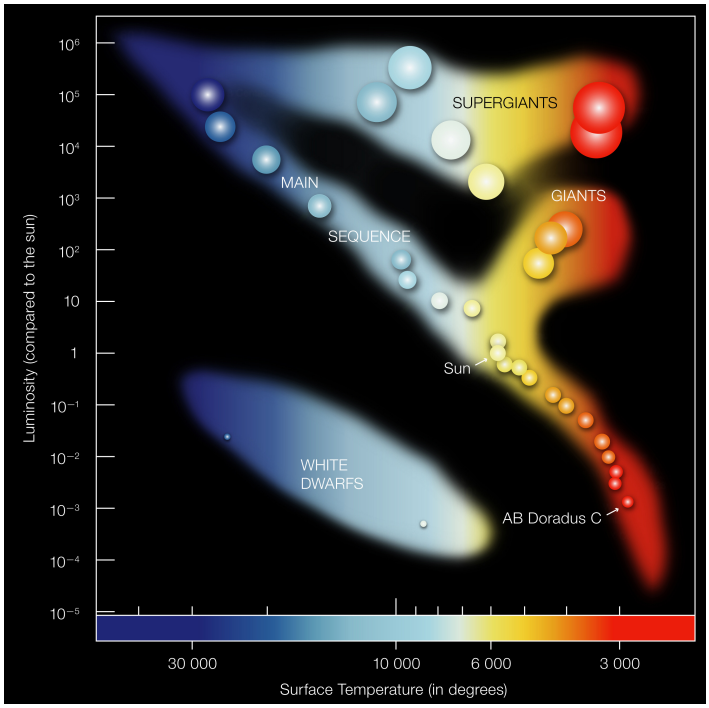


Fig. 1.1: The Hertzsprung-Russell (HR) diagram where the stellar luminosity is plotted against effective temperature. The main sequence, as well as other stages in a star's life cycle is featured in the figure. Image credit: ESO [2], available under a CC BY 4.0 license.

1.2 Red Supergiants

The Red Supergiant (RSG) phase represents a brief but critical late-stage evolutionary phase for stars with initial masses of about $8 - 40\ M_\odot$ [3]. Before entering the RSG stage, these stars spend $\sim 10^6 - 10^7$ years on the main sequence fusing hydrogen [3]. Once core hydrogen is depleted, the stars undergo a rapid expansion and cooling of the outer envelope as they transition to core helium burning. This will cause them to move horizontally across the HR diagram toward the upper-right corner, which is a region characterized by high luminosity and low temperature. This movement is bounded by the *Hayashi Limit*, a theoretical threshold that defines the coolest temperature a star in hydrostatic equilibrium can maintain [3]. As the stars approach this limit, the evolution proceeds at approximately constant temperature while the radius and luminosity continue to increase gradually. It is during this phase that these stars are classified as red supergiants, the "red" part of the name refers to the cool temperature of these stars. The combination of their low temperature ($\sim 3500 - 4000$ K) and high luminosities ($\sim 1400 - 200\,000\ L_\odot$) makes them among the largest known stars in terms of radius ($\sim 100 - 1000\ R_\odot$) [3].

A defining feature of the RSG phase is the extensive circumstellar dust and high mass-loss rate [3]. The mass loss is mainly a result from the exceptionally low surface gravity, allowing stellar winds to escape more easily. While the physical mechanisms that drive this mass loss are still unclear, it is evident that this process contributes to the dust content and chemical enrichment of the interstellar medium. As the mechanism behind the RSG mass loss remains a subject of active research, many studies utilize observations of RSGs circumstellar environments. Multi-wavelength observations reveal excess of circumstellar dust around the stars as well as the dust being distributed in shells [3]. The structural evidence of these shells suggests that mass loss is not always a steady wind, and that it instead can be episodic [3].

1.3 Young Massive Star Clusters

Star clusters are gravitationally bound groups of stars that are formed from the same molecular cloud. The stars are therefore born roughly at the same time and lie approximately at the same distance from Earth [4]. Clusters are generally categorized into two main types, *Open clusters* and *Globular clusters* [4]. Open clusters are relatively loosely bound clusters, containing tens to a few thousands of young and relatively low mass stars and are mostly situated in the galactic disc [4]. In contrast, globular clusters have a more spherical structure containing upwards of 10^5 tightly bound old and massive stars with a higher concentration of stars towards its center [4]. These clusters are primarily found in the galactic halo.

Another type of clusters are *young massive clusters* (YMCs) which fills the gap in between the open clusters and globular clusters. These are clusters with ages comparable to open clusters but their masses and densities exceed those of open clusters found in the Milky Way [5]. The evolutionary phases of a YMC is usually defined into three phases. In the first phase it is still forming stars and the cluster contains significant amounts of ambient gas [5]. The second phase starts roughly when the first supernovae appear in the cluster, which is ~ 3 Myr after the cluster formation [5]. During this phase, the residual molecular gas is cleared from the cluster through a combination of stellar feedback mechanism including stellar winds, ionizing radiation and energy released from supernova explosions. This gas expulsion causes the cluster to expand and can, in some cases, lead to its complete dissolution [5]. The second phase ends when the stellar mass loss diminishes and the cluster either expands until it completely dissolves or until the cluster core starts to contract again, at which point the third phase begins. During this phase, stellar dynamical processes dominate the long-term evolution of the cluster [5]. The dividing line between the second phase and the third can be anywhere between 100 Myr and 1 Gyr, depending on factors such as initial mass, radius, and density profile of the cluster [5].

Zwart et al. [5] discuss that clusters can form through merges of smaller sub-clusters. Studies have shown that star formation in clusters that are still embedded in their molecular cloud does not necessarily occur as a single event. Instead the cloud can form stars in a hierarchal fashion and therefore some kind of merging has to occur during the early evolution [5]. Moreover, the authors also mention *mass segregation*, where more massive stars form closer to the center, which is consistent with what simulations show. Beyond mass segregation in the early evolution, Zwart et al. [5] suggest that mass segregation could also happen during phase 2 when the cluster expands because of stellar mass loss. An unsegregated cluster can still undergo mass segregation during the period when the residual gas is being ejected.

Phase 2 is particularly significant for clusters hosting RSGs as their extremely high mass-loss rates driven by strong stellar winds aid the clearing of molecular gas [5]. However, studying RSGs in this phase has historically been difficult due to their short evolutionary timescales, but in the past decade, a significant population of RSGs has been discovered within YMCs near the Galactic center [3]. Specifically, five RSG clusters (RSGC) have been found near the base of the Scutum-Centaurus arm, known as RSGC1 to RSGC5 [3]. These clusters host at least 76 RSGs, making this the most RSG rich region known in the Milky way [3]. This concentration suggests that there has been a recent and massive burst of star formation in this specific region of the galaxy.

Notably, RSGC1–3 have estimated ages of $12 - 18$ Myr (see Table 2 in Zwart et al. [5]) placing them well into the second phase of their evolution. At this stage, most massive stars have already evolved and exploded as supernovae, leaving behind less massive RSGs. The observed gas distribution will therefore reflect the history of stellar feedback from both supernova explosions

and ongoing mass loss from the present day RSGs. Yet, despite the high density of RSGs in this region, there are only around a few hundred RSGs that have been discovered while population predictions suggests there should be a several thousand RSGs in the Milky Way [3].

1.4 The Stephenson 2 Cluster

The five clusters that have been discovered are prominent examples of YMCs, among these clusters is Stephenson 2, also known as RSGC2. This is a young, massive cluster containing 26 RSGs and is a strong candidate to be the most massive cluster in the Galaxy [6]. The age of RSGC2 has been estimated at $\tau = 17 \pm 3$ Myr and it is located at a distance of ~ 6 kpc from Earth[6]. Many studies have been trying to learn more about the structure of this cluster and its RSGs. For instance, several studies have attempted to measure the radial velocity of the whole cluster itself. Using near infrared spectroscopy of individual RSG members, Davies et al. [7] found the mean Local Standard of Rest (LSR) velocity to be $v_{\rm LSR} = 109.3 \pm 0.7$ km/s. In contrast, Deguchi et al. [8] found a lower value of $v_{\rm LSR} = 96.6$ km/s based on SiO maser emission lines associated with four cluster members. Furthermore, Deguchi et al. [8] also suggested that a group of sources located southwest of the cluster are too far away from the cluster core to be physically related and should therefore form a different cluster. They name this region as *Stephenson 2 SW*, where SW stands for Southwest. While these sources do exhibit a lower $v_{\rm LSR}$, the authors note that the difference is not sufficiently large to actually rule out a physical association with the main cluster. Additionally, their analysis of CO ($J = 1 \rightarrow 0$) line emission revealed that RSGC2 is associated with a significant reservoir of molecular gas, providing further insight into the star-forming history.

Fig. 1.2 shows three plots of RSGC2, each highlighting different structures in RSGC2. The first two plots display the cluster and its immediate surroundings with white markers for stars that reside in the cluster core and red for stars in the proposed SW region. The third plot focuses on just the extent of the RSGs where the individual stellar positions are labeled with their respective numbers. Different studies have used different numbering for the stars, here, the numbering from Davies et al. [7] is used. To avoid confusion, designations from Davies et al. [7] are often given a prefix of DFK which will be used in this study. Out of these stars, the most notable is DFK 1 (also known as St2-18 [8]) which is the brightest star in the cluster and shows a radial velocity that differs from the other stars. It has been suggested that this star might be a foreground giant, however Davies et al. [7] suggest that it is likely a cluster member whose measured velocity is offset by an optically thick expanding envelope, consistent with the outflow speeds of extreme mass-losing RSGs [7].

The left plot highlights three objects identified by Davies et al. [7] in their infrared investigation of the region surrounding RSGC2. These objects are named after the *Infrared Astronomical Satellite (IRAS)* catalog in which they were first recorded [9]. Davies et al. [7] hypothesize that these IRAS sources are further evidence of recent starburst activity. Specifically, *IRAS 18369-0557* appears as a ring of material lacking any central source, suggesting it may be a supernova remnant. Another ring-shaped structure is *IRAS 18367-0556* (also known as *GPRS5 26.316-0.012*), which features a highly reddened star in the center, reminiscent of an evolved star surrounded by the ejecta of a previous high-mass-loss phase. A feature towards the center of RSGC2, *IRAS 18364-0605*, is interpreted as a bow-shock structure likely associated with a specific star (DFK 49) [7].

Four more structures have been identified in this study by using far-infrared data from Herschel/PACS, denoted here as PACS-A, PACS-B, PACS-C and PACS-D (discussed further in Section 5.2). These sources were not identified in the original Davies et al. [7] paper, as the

Herschel/PACS dataset was not available at that time. Another way to visualize the Herschel/-PACS dataset is via the middle figure which shows the same field of view as the first plot, but displaying only the Herschel/PACS 160 μm continuum emission. This is a separate dataset, observed at longer wavelengths than the left plot. These three figures will be frequently used in the analysis of this thesis and will be referred back to when relevant.

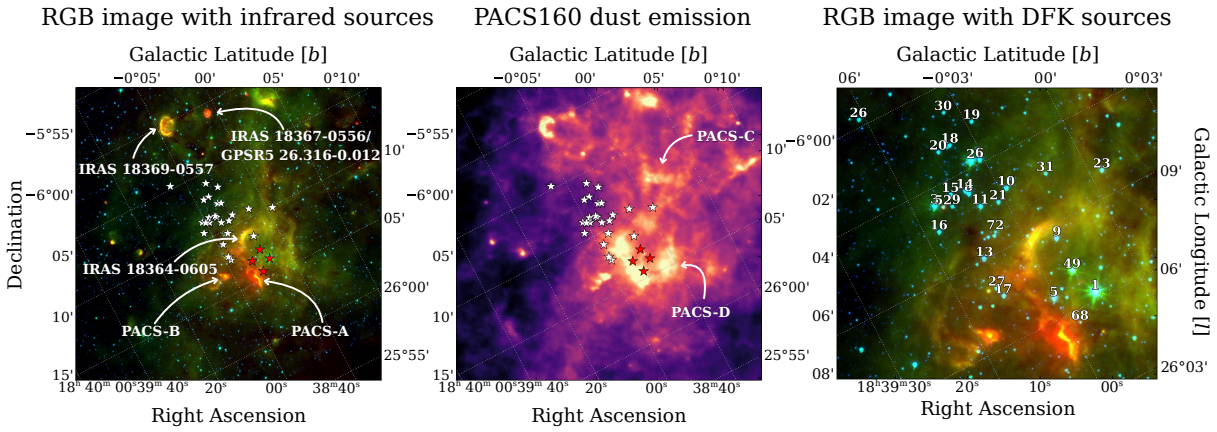


Fig. 1.2: The left and right panel show a multi-wavelength RGB image of RSGC2 constructed using the Herschel/PACS 70 μm (red), GLIMPSE 8 μm (green) and GLIMPSE 3.6 μm (blue). The left plot shows a wide-field view including the IRAS features (IRAS 18369-0557, 18367-0556, and 18364-0605) identified by Davies et al. [7] and PACS-A and PACS-B identified in this study. The middle plot shows the cold dust emission from the Herschel/PACS 160 μm continuum emission data where PACS-C and PACS-D are highlighted. The right panel provides a more concentrated view of the cluster core with the DFK numbering system for the sources from Davies et al. [7]. For the left and middle figure, the stellar positions are marked with white and red star symbols for the cluster core and the SW members, respectively.

1.5 Aim and Outline

The primary aim of this thesis is to characterize the interstellar environment surrounding RSGC2 by separating cluster-associated material from unrelated foreground Galactic structures along the line of sight. This includes an investigation into the connection between the cluster core and the proposed South-West sub-cluster. This characterization is achieved through a multi-wavelength analysis of the molecular gas via various CO emission lines and dust emission via infrared data. To accomplish this, the research is executed across three primary objectives. First, mapping the spatial and kinematic distribution of molecular structures along the line of sight toward RSGC2 using large-scale public surveys to enable a clear kinematic separation between cluster-associated material and unrelated foreground structures. Secondly, investigating the physical nature and association of several infrared sources, including previously identified IRAS sources and newly identified far-infrared structures. Lastly, assessing whether the kinematic and structural evidence supports the hypothesis that the SW stellar population constitutes a distinct sub-cluster within the broader RSGC2 environment.

This thesis is organized as follows. Chapter 2 presents the theoretical background necessary to contextualize the results of this study, covering the interstellar medium and its molecular gas tracers, interstellar dust, and the fundamental concepts of radio astronomy. Chapter 3 describes the observational data and methodology used in this study. Chapter 4 presents the observational results, including a analysis of the molecular gas along the line of sight toward RSGC2, followed

by the moment 0 maps and channel maps in different velocity ranges. Chapter 5 discusses the physical implications of these results, examining the nature and association of the identified infrared sources as well as the evidence for a molecular gas barrier separating the cluster core from the South-West sub-cluster. This chapter also outlines directions for future work before a summary of the main findings of the thesis are presented in Chapter 6.

2

Theory

This chapter outlines relevant theory required to interpret the observational data and analysis presented in this thesis. First, Section 2.1 establishes the Galactic coordinate systems, while Section 2.2 provides an overview of the Milky Way and its spiral arms. Section 2.3 reviews the physics of the interstellar medium and finally, Section 2.4 introduces the principles of radio astronomy followed by Section 2.5, which details the key observable quantities.

2.1 Coordinates of our galaxy

To study the stars and our galaxy it is often useful to describe the position of the stars. There are many ways to do this, one way is by the so called *celestial coordinates* [4]. This comes from the fact that the sky appears as a spherical surface, which makes it possible to assign a position on the so called celestial sphere with a longitude and latitude. The coordinate that corresponds to longitude is called the right ascension (RA) and is expressed in hours rather than degrees [4]. The coordinate corresponding to latitude is called declination (Dec) and is expressed in degrees [4]. The celestial coordinates are only useful when stars are observed from Earth.

To evaluate objects within a wider galactic context, the *galactic coordinates* are utilized instead [4]. This system defines positions using galactic longitude (l) and galactic latitude (b), where they are both expressed in degrees. By definition, the galactic mid-plane rests at $b = 0°$, and the direction pointing from the Sun toward the Galactic Center is designated at ($l = 0°$, $b = 0°$). In some practices, it can be useful to divide the Milky Way into four galactic quadrants. In such instances, the Sun is set to be the pole of the mapping system instead of the Galactic Center. This is because of practical reasons, since all observations have been done from Earth or within the solar system (as of now). The galactic quadrants are divided as, 1st galactic quadrant ($0° \leq l \leq 90°$), 2nd galactic quadrant ($90° \leq l \leq 180°$), 3rd galactic quadrant ($180° \leq l \leq 270°$), and 4th galactic quadrant ($270° \leq l \leq 360°$). All five of the known RSGCs (RSGC1 to RSGC5) lie within the 1st galactic quadrant, including RSGC2 which resides at coordinates $l = 26.2°, b = -0.1°$ [6].

2.2 The Milky Way and Its Spiral Arms

The Milky Way is a spiral galaxy consisting of several hundred billion stars, one of which is the Sun [10]. The Galactic Plane is where most of the galaxy's mass lies and the solar system is located approximately $R = 8.15$ kpc from the Galactic Center [11]. Viewing the Milky Way from its interior poses difficulties when observing large-scale structures, such as its spiral arms. This internal viewpoint causes multiple structures situated at different distances to be superimposed along the same line of sight on the sky [11]. Considering the large distances and that dust extinction blocks out most of the Galactic plane at optical wavelengths, mapping the spiral

structures in the Milky Way is a difficult task [11].

Reid et al. [12] analyzed a large number of trigonometric parallaxes associated with high mass star-forming regions. Because these regions are excellent tracers for distance measurements, they reliably map the spiral structures of the Milky Way's spiral arms. The results from Reid et al. [12] strongly suggest that the Milky Way is a four-arm spiral, with some extra arm segments and spurs [11]. In Fig. 2.1 they produced a longitude-velocity map from the CfA CO survey integrated from $b = -1°$ to $+1°$ with the traces of the Sagittarius, Scutum, and Norma arms in the first Galactic quadrant. The line of sight toward RSGC2, which has a longitude of $l \approx 26°$, passes through several Galactic arms.

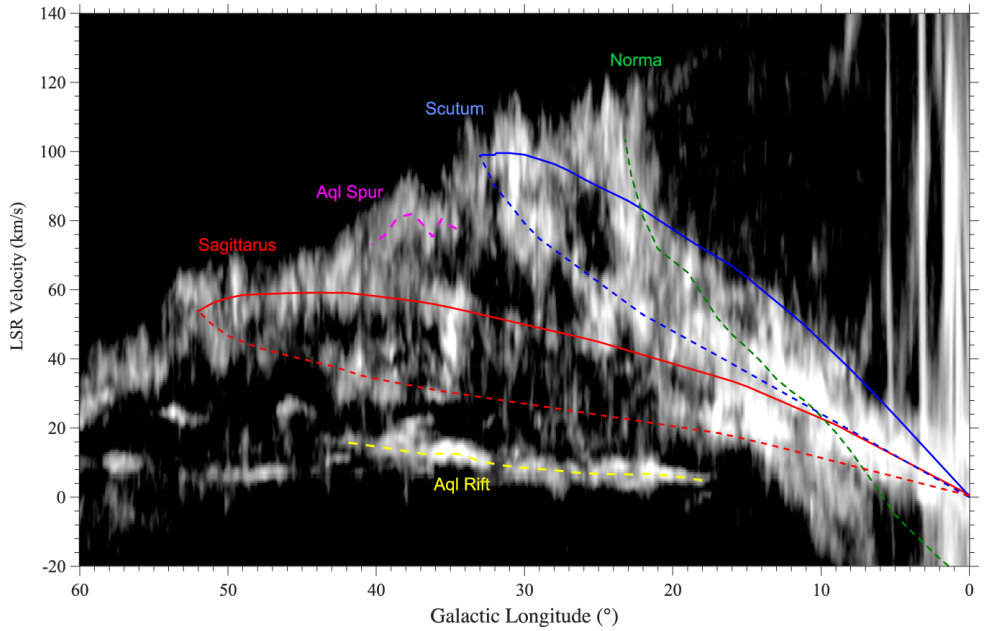


Fig. 2.1: Traces of the Sagittarius, Scutum, Norma and the smaller Aquila spur arms in the first Galactic quadrant. The solid lines indicate the far side of the arms while the dotted lines mark the near sides. The line of sight toward RSGC2, which has a longitude of $l \approx 26°$, passes through several Galactic arms. Figure reprinted from Reid et al. [12]. ©AAS. Reproduced with permission of IOP Publishing. All rights reserved.

2.3 Interstellar Medium

Most of the dust and gas in the Milky Way can be found in the Galactic plane [13]. This gas and dust that lies in between the stars is known as the interstellar medium (ISM) and is crucial because it is the main contribution to star formation [13]. During the evolution of stars and galaxies, the ISM can end up in many different stages. In dense and cold areas of the ISM, it can be gradually converted to stars, in other areas, stars have evolved, and return material to the ISM via stellar winds. This dynamic evolution connects the processes of star formation and stellar feedback, making it a key component in understanding the cycle of matter in the universe. In this cycle, dense molecular clouds collapse to form stars, which over time return material back to the ISM through stellar winds and supernova explosions [1]. This returned material enriches the ISM with metals and dust, which can be incorporated into the next generation of stars. Massive evolved stars, such as RSGs play an important role in this cycle, as their strong stellar winds and high mass-loss rates contributes to the surrounding ISM [13].

2.3.1 CO as a tracer

The ISM exists in several distinct phases, ranging from hot ionized plasma to cold neutral gas. The coldest and densest of these phases is found in molecular clouds, where gas temperatures of $\sim 10-30$ K and high densities allow molecules to form and survive [13]. These clouds represent the reservoir of molecular gas in the galaxy and are predominantly composed of molecular hydrogen (H_2), with carbon monoxide (CO) and other molecules present in smaller but observable quantities [13].

The most common way to study molecular gas is through molecular line emission and the most accessible and widely used tracer is the CO line emission. Despite H_2 being the most abundant molecule in the universe, it lacks a permanent dipole moment, meaning it emits very weakly under the typical cold temperatures of most molecular environments [14]. In contrast, the CO molecule has a small permanent dipole moment and its low-J rotational transitions require low excitation energies. These low-J transitions are also characterized by small spontaneous transition rates (Einstein A coefficients) which allows the transitions to thermalise via collisions with H_2 even in low-density environments [14]. The critical density of the fundamental ^{12}CO $J = 1 \rightarrow 0$ transition at 115 GHz is $n_{\mathrm{crit}} \approx 2.2 \cdot 10^3$ cm^{-3} [14], meaning that the region where this emission is detected has a local particle density that is at least this high.

To map the complex internal structures of molecular clouds, observations must combine multiple CO transitions and isotopologues. Combining multiple tracers helps break degeneracies between temperature, column density and optical depth that would otherwise limit the interpretation of any single tracer. For instance, the ^{12}CO tracer is easily excited in cold, diffuse environments, making it sensitive to extended cloud envelopes [15]. Moreover, as the most abundant isotopologe, ^{12}CO is usually optically thick, meaning its emission only traces the surface or outer part of the molecular cloud [15]. In such cases, to probe deeper into the cloud, other rarer molecular emission can be used, such as ^{13}CO or C^{18}O. Because ^{13}CO is less abundant, it remains optically thin across a wider range of molecular cloud conditions, providing a more accurate probe of the cloud's internal structure [15]. However, in sufficiently dense regions, even ^{13}CO can become optically thick [15].

It is also valuable to study the line intensity ratio of different isotopologues, such as ^{12}CO/^{13}CO which provides information about the chemical evolution of the source as well as serving as an optical depth diagnostic. This is because ^{12}CO is almost always optically thick, causing its emission to saturate and no longer reflect the true amount of gas along the line of sight. ^{13}CO is typically optically thin so it traces the full column of gas and the observed intensity ratio will thus be smaller than the true isotopic abundance ratio [16]. In the local ISM, this true ratio is ~ 70 and it decreases toward the Galactic center as a result of increased stellar processing [16]. As a result, the ratio for the Galactic center is ~ 20 [16]. A ratio that is significantly lower than the expected value indicates that ^{12}CO is optically thick.

Higher-J transitions (e.g $J = 2 \rightarrow 1$, $J = 3 \rightarrow 2$) provide further constraints on the gas physics as they require both warmer temperatures and higher densities to be excited [15]. The line intensity ratio between different transitions, such as ^{12}CO(3-2)/^{12}CO(1-0), can provide useful diagnostics of the molecular gas. Since, $J = 3 \rightarrow 2$ requires higher excitation conditions than $J = 1 \rightarrow 0$, a higher ratio indicates warmer and denser gas, while lower is consistent with diffuse and cold conditions. Together, analyzing multi-line and multi isotopologe datasets simultaneously provides a more complete characterization of the molecular gas.

2.3.2 Interstellar Dust

Interstellar dust is another important component in the ISM as it plays a crucial role in galactic evolution. The most direct way to study interstellar dust is through observations of its interactions with electromagnetic radiation. One such method is via *extinction*, which is the absorption and scattering of electromagnetic radiation by dust between a source and the observer [13]. This can also be called *reddening*, which occurs because the interstellar dust absorbs and scatters blue light waves (shorter wavelength) more than red light waves (longer wavelength), making stars appear redder than they are [13]. The efficiency of dust extinction is highly wavelength-dependent, decreasing significantly towards longer wavelengths. This allows infrared observations to penetrate dense, obscured regions, such as the Scutum-Crux arm, that are opaque in the optical regime.

Similar to the molecular gas, when dust grains get heated by starlight, they cool by radiating in the infrared [13]. By doing so, they reach a state of thermal equilibrium where they re-emit energy at infrared and sub-milimeter wavelengths. In thermal equilibrium, the radiation field becomes the "blackbody" radiation field, with intensity given by the blackbody spectrum,

$$B_\nu(T) = \frac{2h\nu^3}{c^2}\frac{1}{e^{h\nu/kT}-1} \tag{2.1}$$

where ν is the frequency and T is the dust temperature [13]. This approximation is valid for the "classical" grains which are defined as grains with radii $a \gtrsim 0.03\mu$m [13]. Smaller grains have fluctuating temperatures and the blackbody approximation is not applicable. Moreover, according to Wien's displacement law, the peak of the emission shifts to shorter wavelengths as the temperature increases. Thus, "warm" dust ($\sim 50-100$ K) emits more strongly in the mid-infrared ($\sim 5-35$ µm) while "cold" dust ($\sim 10-30$ K) peaks at far-infrared or sub-millimeter ($\sim 35-300$ µm) regime [13][17].

2.4 Radio Astronomy: Radio Telescope and Interferometers

Radio astronomy is the study of radio emission from distant sources. It has enabled the detection and mapping of molecular line emission across the Galaxy, making it an essential tool for studying cool ISM and molecular gas. There is however only a range of frequencies that can be observed, called the *radio window* [15]. The most traditional radio telescopes are so-called *single-dish* telescopes, which utilize a circular parabolic reflector to focus radiation into a receiver [18]. Their ability to create images with great resolution are fundamentally limited by diffraction, and can be approximated by the Rayleigh criterion,

$$\theta \approx 1.22\frac{\lambda}{D}$$

where θ is the angular resolution, λ is the observing wavelength and D is the diameter of the aperture [18]. From this equation, it is clear that achieving high angular resolution with a single-dish telescope requires either observing at short wavelengths or using an exceptionally large diameter D. However, due to physical limitations, the diameter of single-dish telescopes cannot be increased indefinitely [18]. To solve this problem, the interferometer was introduced. In an interferometer, signals from two or more telescopes are combined to synthesize an aperture equivalent to the maximum distance (baseline) between the telescopes, allowing for incredibly high angular resolution that exceeds the capabilities of any single dish instrument [15]. Unlike single-dish telescopes, an interferometer samples specific spatial frequencies in the so-called uv-plane. This means that the shape and size of the resulting synthesized beam are highly sensitive

to the number of antennas in the interferometer and their specific geometric configuration during the observation [15].

Another limitation of interferometric observations is the phenomenon known as *spatial filtering*. Because an interferometer only samples a limited range of spatial frequencies determined by the baseline, it is insensitive to emission on angular scales larger than those probed by the shortest baseline [15]. This results in missing flux from extended sources, causing the measured brightness temperature to be lower than the intrinsic brightness temperature of the source [15]. This effect is relevant when comparing interferometric and single-dish observations.

2.5 Radio Observable Quantities

The data from radio telescopes and interferometers can be expressed in several different, related quantities. The following sections define these fundamental quantities and the mathematical relationships used to convert raw telescope power into physically meaningful units.

2.5.1 Flux Density and the Jansky

One way to measure the strength of a radio source is via *flux density*, S_ν. This is a quantity that is dependent on the distance to the source and is used to characterize unresolved sources [18]. This means that the source is much smaller than the angular resolution of the observing telescope. The units of flux density are W m^{-2} Hz^{-1}, however, since these are large for astronomical sources, the Jansky (Jy) is commonly used instead [18],

$$1 \text{ Jansky } (1 \text{ Jy}) = 10^{-26} \frac{\mathrm{W}}{\mathrm{m}^2 \ \mathrm{Hz}}.$$

The relationship between flux density and specific intensity or brightness, I_ν, is given by [18],

$$S_\nu = \int_{\text{source}} I_\nu(\theta, \phi) \cos\theta \ \mathrm{d}\Omega.$$

For sources with angular sizes $\ll 1$ rad and $\cos\theta \approx 1$, the cos term in the above equation can be neglected. The flux density can thus be expressed much simpler as, $S_\nu \approx \int I_\nu(\theta, \phi) \ \mathrm{d}\Omega$. This is usually the case for astronomical sources, and flux density is rarely used to describe sources so extended that the cos factor must be kept [18]. For extended sources such as a molecular clouds, however, it is more appropriate to characterize the emission in terms of brightness temperature.

2.5.2 Brightness Temperature

The intensity of a source can be expressed in terms of an equivalent temperature, known as the *brightness temperature*, T_b. This brightness temperature is not the same as the physical temperature of the source, instead it is defined as the temperature a blackbody would produce at the same intensity at a given frequency [18]. This temperature is derived by applying the Rayleigh-Jeans approximation to the Plank function (Eq. (2.1)), and takes the form

$$B_\nu(T) \approx \frac{2kT\nu^2}{c^2} \quad \Rightarrow \quad T_b = \frac{I_\nu c^2}{2k\nu^2}. \tag{2.2}$$

This approximation is valid for $h\nu \ll kT$, which is typically the case in the radio regime [18]. This indicates that the brightness temperature varies with frequency but is independent of distance. It is therefore often convenient to express the spectral brightness I_ν in terms of brightness temperature, even if $I_\nu \neq B_\nu$, as this provides an intuitive measure of source intensity that is independent of distance [18].

Using this definition of brightness temperature, it is possible to relate T_b to S_ν. In radio images, it is common to measure I_ν in terms of flux density per main beam (main beam for single dish telescopes and synthesized beam for interferometers.) and it is therefore possible to write, $I_\nu = S_\nu/\Omega_\mathrm{beam}$, where the unit for S_ν is in Jy. Both flux density and the solid angle of the source scale with $1/d^2$, where d is distance, and thus, the resulting brightness temperature will remain distance-independent [15]. The brightness temperature can now be written as

$$T_\mathrm{b} = \frac{\lambda^2}{2k}\frac{S_\nu}{\Omega_\mathrm{beam}}$$

where $\lambda = c/\nu$ [19]. The beam solid angle can in turn be approximated with the area of a Gaussian beam,

$$\Omega_\mathrm{beam} = \frac{\pi}{4\ln 2}\theta_\mathrm{maj}\theta_\mathrm{min}$$

where θ_maj and θ_min are the half-power beam widths along the major and minor axes. Inserting this approximation and converting all constants leads to

$$T_\mathrm{b} = 0.32 \times 10^{23}\frac{\lambda^2}{\theta_\mathrm{maj}\theta_\mathrm{min}}S_\nu \ .$$

Here, the beam widths are given in radians and by converting it to arcseconds while rewriting the expression in terms of frequency instead, the relation becomes

$$T_\mathrm{b} = 1.223 \times 10^{6}\frac{1}{\nu^2\theta_\mathrm{maj}\theta_\mathrm{min}}S_\nu \ . \tag{2.3}$$

2.5.3 Antenna temperature

A useful unit for the spectral power output from a receiving antenna is the *antenna temperature*, T_A [18]. This temperature does not represent the actual temperature of the antenna, instead it is related to the power delivered to the receiver. This definition relies on the *Nyquist theorem*, which is valid for $h\nu \ll kT$ and states that the spectral power generated by a resistor at a temperature T is, $P_\nu = kT$ [18]. Consequently, the antenna temperature is defined as,

$$T_\mathrm{A} = \frac{P_\nu}{k}.$$

T_A can also be written as a relation to the specific intensity of the source, I_ν, through the antenna's *effective aperture*, A_e,

$$T_\mathrm{A} = \frac{A_e}{2k}\iint I_\nu(\theta,\phi)P_n(\theta,\phi)\,\mathrm{d}\Omega$$

where P_n is the normalized power pattern [15]. Using Eq. (2.3) it is therefore also possible to relate the antenna temperature to the brightness temperature. It is important to note that the quantity T_A does not correct for ohmic losses, or atmospheric absorption. To facilitate comparison between different observations, the *corrected antenna temperature* T_A^* is used. This value has been corrected for atmospheric absorption and telescope efficiencies, representing the signal as it would be measured outside the Earth's atmosphere [15].

2.5.4 Main beam brightness temperature

While T_A^* is a useful unit for comparison between different observations, it is still dependent on the specific power pattern of the telescope, P_n. To obtain a value that represents the intrinsic brightness of the source, the *main beam efficiency*, η_mb must be taken into account. The main

beam efficiency represents the fraction of the antenna power pattern concentrated in the main beam compared to the total power received [15]. This efficiency essentially defines the quality of an antenna as a direction measuring device. As a result, the *main beam brightness temperature* is defined as,

$$T_{\mathrm{mb}} = \frac{T_{\mathrm{A}}^{*}}{\eta_{\mathrm{mb}}}. \tag{2.4}$$

For extended sources that fill the main beam, such as large molecular clouds, T_{mb} provides the most accurate representation of the gas brightness temperature. Most thermodynamic equations in the ISM assume the use of T_{mb} or T_{b} [15].

3

Observational Data and Methods

The objective of this chapter is to present the outline of the analysis techniques that were used to characterize the molecular gas environment of RSGC2. First in Section 3.1, the observational surveys and their respective data modifications are detailed. This is followed by Section 3.2 that describes the velocity integration ranges used to isolate discrete Galactic structures. Finally, the imaging and mapping methodologies used to generate the figures are described in Section 3.3, 3.4, 3.5 and 3.6. The analysis combines molecular line emission and dust continuum imaging to characterize the interstellar environment of RSGC2. Molecular gas is traced through CO spectral line emission while dust emission is visualized through infrared continuum imaging. These two tracers are used in a complementary manner where integrated intensity maps (Section 3.5) are overlaid on a dust continuum image (Section 3.6) to identify spatial correlations between cold gas and dust structures, providing a two-dimensional view of the cluster environment. Additionally, velocity-resolved channel maps (Section 3.4) are overlaid on a multi-wavelength composite RGB image (Section 3.6) to investigate the kinematic association of molecular gas with specific infrared features, enabling a three-dimensional perspective of the line of sight structures.

To process and visualize these diverse datasets, a custom Python pipeline was developed using primarily the `astropy` [20] and `spectral-cube` [21] packages. This python pipeline developed in this thesis is publicly accessible via GitHub. Moreover, the pipeline also features interactive widgets for a more dynamic examination of the cluster environment. While these interactive tools and plots are not displayed in this thesis, the source code is available in the repository.

3.1 Surveys

This study compiles observations from several different independent studies and each set needed to be processed in various ways to ensure comparability. As outlined in Table 3.1, the observations can be categorized into two groups: molecular line spectral cubes and continuum (dust) imaging. For stellar scale investigation of circumstellar environments, high-resolution CO emission data were extracted from the Atacama Large Millimeter/sub-millimeter Array (ALMA) [22]. For the large scale analysis of molecular line emission, spectral cubes from the public surveys Galactic Ring Survey (GRS) [23], FUGIN [24], and ^{12}CO High-Resolution Survey (COHRS) [25] were utilized. Complementary dust emission data were obtained from the public Galactic Legacy Infrared Midplane Survey Extraordinaire (GLIMPSE) [26] and Herschel infrared Galactic Plane Survey (Hi-GAL) [27]. The technical specifications and specific modification steps for each data source are detailed in the sections below.

Table 3.1: Summary of the radio, millimeter, and infrared datasets utilized in this study, including their primary tracers, velocity coverages and angular resolution.

Survey Name	Primary Tracer	Data Type	Velocity Range	Angular Res.
ALMA	^{12}CO, ^{13}CO ($J = 2 \rightarrow 1$)	Spectral Cube	-86 – 180 km/s	$\sim 0.4''$
GRS	^{13}CO ($J = 1 \rightarrow 0$)	Spectral Cube	-5 – 200 km/s	$46''$
FUGIN	^{12}CO, ^{13}CO, C^{18}O ($J = 1 \rightarrow 0$)	Spectral Cube	-100 – 200 km/s	$20''$
COHRS	^{12}CO ($J = 3 \rightarrow 2$)	Spectral Cube	-200 – 300 km/s	$14''$
GLIMPSE	Mid-IR Continuum (3.6–8.0 μm)	2D Image	-	$\sim 2''$
Herschel/PACS	Far-IR Continuum (70–160 μm)	2D Image	-	$5.6''$

3.1.1 ALMA

ALMA is an interferometer situated in the Atacama Desert in Chile and is composed of 66 high-precision antennas, spread over distances of up to 16 km [22]. It was built to study some of the coldest objects in the universe which radiate in the millimeter and sub-millimeter wavelength regime. Because of its large number of antennas, the antennas can be arranged in different configurations. Its main 12-meter array has fifty antennas, each with a diameter of 12 meter [22]. There is also an additional array with four 12-meter and twelve 7-meter antennas to complement the main array [22].

The ALMA data used in this study targeted the ^{12}CO ($J = 2 \rightarrow 1$) transition at 230.538 GHz for DFK 1, 2, 3, 5, 6, 8, 10, 11, 13, 14, 23, 49, 52 and 68, using the main 12-meter array. For DFK 52, two additional observations were carried out using the Atacama Compact Array (ACA), also known as the 7-meter array. These observations used an extended spectral tuning that simultaneously covered both the ^{12}CO ($J = 2 \rightarrow 1$) and ^{13}CO ($J = 2 \rightarrow 1$) transitions at the same time. Table 3.2 summarizes the configuration, observations and the values for the synthesized beam.

As seen in Table 3.2, the synthesized beam dimensions vary across different targets because the observations were executed at different times under slightly different configurations. Notably, the ^{12}CO ($J = 2 \rightarrow 1$) and ^{13}CO ($J = 2 \rightarrow 1$) observation of DFK 52 using the 7 meter configuration also have different beam dimensions despite being from the same observation. This is due to the frequency dependence of the synthesized beam which means that the unit "Jy/beam" is inconsistent across the observations. The variations in beam size will have a substantial effect when comparing between different observations and lead to a misrepresentation of line intensities. To mitigate this and establish a uniform intensity scale, the *Common Astronomy Software Applications* (CASA) package[1] was used to convert the pre-calibrated data cubes from flux density (S_ν) to brightness temperature (T_b) via Eq. (2.3), using the respective θ_min and θ_max values listed in Table 3.2 at the rest frequency, $\nu = 230.538$ GHz.

[1]CASA is the primary data processing software for ALMA. In this study, CASA was used for unit conversion and visualization of the ALMA data, but not for data calibration, which was performed prior to this study.

Table 3.2: A summary of the different observations, configurations, and size of the synthesized beam for each source.

DFK	Observation	Configuration	Synthesized beam
1	^{12}CO ($J = 2 \rightarrow 1$)	12m	$0.50'' \times 0.36''$
2	^{12}CO ($J = 2 \rightarrow 1$)	12m	$0.50'' \times 0.36''$
3	^{12}CO ($J = 2 \rightarrow 1$)	12m	$0.45'' \times 0.32''$
5	^{12}CO ($J = 2 \rightarrow 1$)	12m	$0.51'' \times 0.37''$
6	^{12}CO ($J = 2 \rightarrow 1$)	12m	$0.41'' \times 0.31''$
8	^{12}CO ($J = 2 \rightarrow 1$)	12m	$0.41'' \times 0.31''$
10	^{12}CO ($J = 2 \rightarrow 1$)	12m	$0.41'' \times 0.31''$
11	^{12}CO ($J = 2 \rightarrow 1$)	12m	$0.41'' \times 0.31''$
13	^{12}CO ($J = 2 \rightarrow 1$)	12m	$0.41'' \times 0.31''$
14	^{12}CO ($J = 2 \rightarrow 1$)	12m	$0.41'' \times 0.31''$
23	^{12}CO ($J = 2 \rightarrow 1$)	12m	$0.41'' \times 0.31''$
49	^{12}CO ($J = 2 \rightarrow 1$)	12m	$0.50'' \times 0.36''$
52	^{12}CO ($J = 2 \rightarrow 1$)	12m	$0.46'' \times 0.32''$
52	^{12}CO ($J = 2 \rightarrow 1$)	12m+7m	$0.46'' \times 0.33''$
52	^{12}CO ($J = 2 \rightarrow 1$)	7m	$4.03'' \times 2.99''$
52	^{13}CO ($J = 2 \rightarrow 1$)	7m	$4.15'' \times 3.22''$
68	^{12}CO ($J = 2 \rightarrow 1$)	12m	$0.46'' \times 0.32''$

3.1.2 Galactic Ring Survey

The Galactic Ring Survey, also known as The Boston University-Five College Radio Astronomy Observatory Galactic Ring Survey (GRS) was a survey that targeted emission from ^{13}CO ($J = 1 \rightarrow 0$) at 110.291 GHz in the Milky Way [23]. This survey used a multi pixel array on the Five College Radio Astronomy Observatory 14 m telescope to cover a longitude range of $l = 18^\circ - 55.7^\circ$, a latitude range of $|b| < 1^\circ$ and a velocity range of $-5 - 135$ km/s [23]. Because of its large scale, this survey was used to analyze the wide scale of the cluster. The data was given in corrected antenna temperature, T_A^*, which had to be converted into main beam temperature, T_{mb}, using Eq (2.4) where $\eta_{mb} = 0.48$ [23].

3.1.3 FUGIN

The FUGIN survey used a new Four-beam Receiver System on the Nobeyama 45 m telescope (FOREST) [24]. This survey targeted the $J = 1 \rightarrow 0$ transition of the three CO isotopologues, ^{12}CO, ^{13}CO and C^{18}O. The observed regions spanned portions of the first quadrant ($10^\circ \leq l \leq 50^\circ, |b| \leq 1^\circ$) and the third quadrant ($198^\circ \leq l \leq 236^\circ, |b| \leq 1^\circ$) of the Galaxy. This survey was used for the large scale analysis and because the intensities were provided directly in main beam temperature, T_{mb}, no additional modifications were required. While the initial data analysis was done on all three molecular lines, the C^{18}O emission was affected by noise in the RSGC2 region and not much could be seen within that data cube. It was therefore omitted from the final results.

3.1.4 COHRS

The last large scale data survey for molecular line emission is the ^{12}CO (3–2) High-Resolution Survey (COHRS) which was carried out using the Heterodyne Array Receiver Program on the 15 m James Clerk Maxwell Telescope in Hawaii [25]. As specified in the name, it targeted ^{12}CO ($J = 3 \rightarrow 2$) at 345.786 GHz. This survey mapped the inner Galactic plane with a longitude range of $9.5° \leq l \leq 62.3°$ and latitude, $|b| \leq 0.5°$. The public data release was partitioned into 106 discrete tiles with a 0.5° longitude width and 1° latitude length [25]. Therefore, when plotting a wide-field view, two tiles had to be joined together to get the larger picture. Moreover, this dataset, similar to GRS, was given in corrected antenna temperature, $T_{\rm A}^*$, and had to be converted to main beam temperature, $T_{\rm mb}$, using Eq (2.4) where $\eta_{\rm mb} = 0.61$ [25].

3.1.5 GLIMPSE

The Galactic Legacy Infrared Mid-Plane Survey Extraordinaire (GLIMPSE) was a legacy program carried out by NASA's Spitzer Space Telescope [26]. This study utilizes data specifically from the GLIMPSE I survey, which mapped the inner Galactic plane across the longitudes, $10° \leq l \leq 65°$ and $|b| \leq 1°$ [26]. These observations were conducted using The Infrared Array Camera (IRAC) in four mid-infrared bands centered at 3.6, 4.5, 5.8, and 8.0 μm. For this study, only the bands centered at 3.6, 4.5 and 8.0 μm were used. For the rest of this thesis, the dataset corresponding to each band will be noted as, I1 (3.6μm), I2 (4.5μm) and I4 (8.0μm).

3.1.6 Herschel/PACS

To complement the GLIMPSE survey and its mid-infrared data, far-infrared observations were obtained from the Herschel Space Observatory archive. Specifically, data from the Photodetector Array Camera and Spectrometer (PACS) were utilized, with two broad bands centered at 70 and 160 μm [28]. The datasets for these two bands are called PACS70 (70μm) and PACS160 (160μm).

3.2 Velocity Ranges

To efficiently isolate, identify and map discrete Galactic structures along the line of sight, the data cubes were divided into distinct velocity windows. The velocity limits for these windows were determined based on the expected radial velocities of the various spiral arms intersecting the line of sight towards RSGC2 ($l \sim 26°$). For the outer arm, the velocity range was extracted from figure 3 in Dame et al. [29]. For the remaining spiral arms, Fig. 2.1 by Reid et al. [12] was used to identify velocities that coincided with the cluster's Galactic longitude. The literature figures provided initial estimates for the central velocity of the spiral arms at the longitude of RSGC2. However, since spiral arms exhibit velocity dispersion and the line-of-sight emission spans a range of velocities, the final velocity boundaries were determined empirically. By examining where distinct emission features appear for each structure in the observed spectral profiles, the velocity ranges were established as follows:

- -25 – -15 km/s: Outer arm
- 3 – 17 km/s: Aql Rift
- 23 – 35 km/s: Sagittarius Arm (near side)
- 45 – 60 km/s: Sagittarius Arm (far side)
- 67 – 81 km/s: Scutum Arm (near side)
- 90 – 115 km/s: Scutum Arm (far side) and Cluster velocity.

These windows, along with the initial central velocity read from the literature plots, are visually highlighted as shaded regions and black dotted lines, respectively, in Fig. 4.1. Regarding the cluster velocity, as noted in Section 1.4, a consensus value for v_{LSR} remains elusive as different studies have reported on different values. In this study, the cluster velocity has therefore been defined as a range between $90 - 115$ km/s.

While there are several arms that can be identified in these velocities, not all surveys cover an identical spectral range and hence velocities. As a result, certain structures might not be mapped across every single dataset. Table 3.1 outlines the velocity ranges for each survey, demonstrating that while surveys like ALMA, FUGIN and COHRS capture the Outer Arm, GRS will not cover that.

3.3 Spectral Plot

To obtain an initial overview of the data cubes, one-dimensional spectral profiles were extracted and the temperature was plotted against velocity. For the wide-field single-dish surveys, line intensities are expressed in main-beam brightness temperature (T_{mb}) while for the high-resolution ALMA interferometric cubes, it is expressed in brightness temperature (T_{b}).

Because the spatial coverage varies between surveys, the isolated emission associated with each RSG had to be extracted differently. For the ALMA observations, the spatial coverage is intrinsically centered on each individual source, therefore, the spectra were generated by integrating the brightness temperatures across the entire image for each data cube. On the other hand, the wide-field surveys (GRS, FUGIN, and COHRS) cover large areas of RSGC2. To isolate each source, a circular region with a 20" (arcseconds) radius was defined and centered on the precise coordinate of each DFK source. The coordinates of the sources were taken from table 1 in Davies et al. [7]. Comparing these single dish and interferometric line profiles makes it possible to make a detailed assessment of which molecular structures are traced at different velocities. Note that the ALMA data cube measures a lower brightness temperature due to the spatial filtering. The ALMA line intensities were therefore scaled by a factor of five in Fig. 4.1 to facilitate a more visual comparison of the spectral features across all datasets.

3.3.1 Line intensities and ratios

In addition to the spectral profiles, a mean brightness temperature (T_{b} for ALMA and T_{mb} for the other surveys) can be calculated for each source and each survey by averaging the intensity over a defined velocity range. These mean temperatures can in turn be used to compute molecular line emission ratios between two transitions or isotopologues. Since the ALMA observations are expressed in brightness temperature and the remaining surveys in main beam temperature, the only significant ratios that could be calculated were

$$R_{(3-2)/(1-0)} = \frac{< T_{\mathrm{mb}(^{12}\mathrm{CO}\ J=3\rightarrow 2)} >_v}{< T_{\mathrm{mb}(^{12}\mathrm{CO}\ J=1\rightarrow 0)} >_v} \quad \text{and} \quad R_{12/13} = \frac{< T_{\mathrm{mb}(^{12}\mathrm{CO}\ J=1\rightarrow 0)} >_v}{< T_{\mathrm{mb}(^{13}\mathrm{CO}\ J=1\rightarrow 0)} >_v}. \tag{3.1}$$

$R_{(3-2)/(1-0)}$ and $R_{12/13}$ are defined as the ratios of the averaged intensities of the respective transitions which is denoted by the angle brackets. Each ratio is calculated over the velocity range of interest. Here, ^{12}CO(3-2) is the intensity taken from COHRS, while both ^{12}CO(1-0) and ^{13}CO(1-0) are taken from FUGIN.

Similarly, the averaged main beam temperature and molecular line ratios can also be calculated for the infrared features. This can only be done using the wide-field surveys (GRS, FUGIN,

and COHRS) as ALMA does not cover the positions of the infrared sources. To isolate these five features, circular regions were defined for each feature. The positions and radii of the circle can be found in Table 3.3. The positions of the IRAS sources were taken from the Strasbourg astronomical Data Center[2], where they are listed in the original IRAS Point Source Catalog [30]. For the PACS sources, their positions were estimated by plotting the circular region, ensuring that it covered the whole source.

Table 3.3: Coordinates and radii for the circle region drawn to extract the line intensities.

Sources	Coord (RA)	Coord (Dec)	Radii
IRAS 18369-0557	18h 39m 36.1s	-05d 54m 25s	50”
IRAS 18367-0556	18h 39m 22.8s	-05d 53m 25s	21”
IRAS 18364-0605	18h 39m 09.7s	-06d 03m 22s	45”
PACS-A	18h 39m 05.7s	-06d 06m 55s	50”
PACS-B	18h 39m 16.7s	-06d 06m 43s	30”

3.3.2 Propagation of Uncertainties

When calculating the average line intensity, uncertainties arise from noise in the data cubes. Specifically, the standard deviation was computed over each source using the last 10 line-free channels of each data cube. Since the line ratios are calculated from mean line intensities, the fractional uncertainties add in quadrature. For a ratio $R = A/B$, this is calculated as,

$$\sigma_R = R \times \sqrt{\left(\frac{\sigma_A}{A}\right)^2 + \left(\frac{\sigma_B}{B}\right)^2}$$

where σ_A and σ_B is the uncertainty calculated from the line free channels while A and B are the respective line intensity [31].

For the mean value computed over N individual ratios, the uncertainty of the mean (σ_{avg}) is given by

$$\sigma_{\text{avg}} = \frac{\sqrt{\sigma_1^2 + \sigma_2^2 + \cdots + \sigma_N^2}}{N}$$

where σ_i are the individual uncertainties for each ratio [31].

3.4 Channel Maps

A diagnostic tool to analyze the raw three-dimensional data cubes are channel maps. A channel map consists of a series of two-dimensional spatial images, each representing a narrow, discrete velocity interval (Δv) across a spectral line profile. Because interferometric and single-dish data cubes preserve velocity information, channel maps allow for the visualization of kinematics without losing depth information along the line of sight. In this study, channel maps were essential for identifying distinct velocity components as well as finding structures outside the cluster velocities. However, each data survey has different velocity resolution, and to ensure a comparative analysis, they had to be binned to the one with largest velocity resolution. The survey with largest velocity resolution was ALMA with $\Delta v \approx 1.27$ km/s.

[2] https://cds.unistra.fr/

3.5 Moment Maps

To investigate the spatial distributions of the molecular gas in RSGC2, moment maps were generated from CO data cubes. Moment maps are weighted integrations of the spectral line along the velocity axis, providing a two-dimensional representation of the three-dimensional data [15]. Moment maps are commonly used in radio astronomy and there are several orders of moment maps that showcase different structures. The zeroth moment (M_0) represents the integrated intensity map and is defined as

$$M_0 = \int I_v dv \ .$$

where I_v is the specific intensity at velocity v [32]. As already discussed in the above sections, to ensure comparability, the units for the spectral cubes were converted into brightness temperatures (for ALMA) or main beam temperature (for GRS, FUGIN and COHRS). This means that the integrated intensity map will be defined as

$$M_0 = \int T(v) dv \ .$$

The resulting unit for M_0 is the cube unit times the spectral axis unit, which in this case will therefore be K km/s. This map traces the total gas column density along the line of sight and provides a spatial picture of where the molecular gas is distributed across the cluster. By computing M_0 over specific velocity ranges, such as those mentioned in Section 3.2, emission associated with specific molecular clouds or structures can be isolated from unrelated foreground. This is especially important in crowded sightlines such as RSGC2 where multiple unrelated ISM components may overlap spatially.

3.6 Dust emission images

There are mainly two ways to visualize infrared continuum emission. One way is to plot one dataset by itself, showcasing the dust emission from that specific wavelength. This can be useful when tracing dust within a certain temperature range as colder dust emits at longer wavelengths. Another way to visualize dust emission is through multi-wavelength infrared datasets or, three-color – Red-Green-Blue (RGB) – figures. By assigning a specific infrared band to each primary color channel, blue for shorter wavelengths and red for longer wavelengths, it is possible to qualitatively map the temperature distribution of the ISM. For example, a region appearing blue in such a composite indicates the presence of warm dust heated by nearby massive stars, whereas red structures trace the cold, dense molecular gas where star formation may occur.

The dust emission datasets available for this study are from GLIMPSE and Herschel/PACS. The available datasets for GLIMPSE are bands centered at 3.6, 4.5 and 8.0 μm, which are denoted as I1 (3.6 μm), I2 (4.5 μm), and I4 (8.0 μm). The Herschel/PACS datasets consists of two broad bands centered at 70 and 160 μm denoted as PACS70 (70 μm) and PACS160 (160 μm). These datasets are used to visualize the dust and infrared emission, as illustrated in Section 1.4, Fig. 1.2. The RGB image is constructed using PACS70 for the red channel, I4 for the green channel and I1 for the blue channel, mapping the thermal dust emission from longer to shorter wavelengths across the infrared spectrum. The PACS160 image displays the single wavelength dust continuum emission, tracing the coldest structures in the region. These are the two dust emission images that will used in various ways for the analysis of RSGC2.

4

Results

This chapter presents the observational findings of this study. Section 4.1 details the spectral profile analysis for each source across multiple molecular line surveys and spiral arm velocity ranges. Section 4.2 follows up with the moment 0 maps for four of the galactic spiral arms, Aql Rift, far and near side of the Sagittarius Arm and the near side of Scutum Crux. This section also examines the channel maps of the near side of the Sagittarius arm. Section 4.3 moves away from the foreground spiral arm structures and focuses on the cluster velocity. Here, the moment 0 maps for each survey are presented both as intensity maps and overlaid on the PACS160 dust map. This section also presents the mean brightness temperatures for both the 14 RSGs and the infrared sources as well as the channel maps over the cluster velocity window. Lastly, Section 4.4 presents the two ratios, $R_{(3-2)/(1-0)}$ and $R_{12/13}$.

4.1 Spectral Analysis

The spectral profiles for each targeted source across the five molecular line surveys are presented in Fig. 4.1. The different velocity ranges that represent the individual spiral arms (See Section 3.2) are indicated by the shaded colored regions. The black dotted vertical lines mark the initial estimates for the central velocity from the literature. Overall, the observed spectral profiles align well with the kinematic boundaries of the Galactic spiral arms. A notable exception is the Outer Arm window where a clear emission peak is only detected in the spectral profiles toward DFK 68, 1 and 49. The spectra for ALMA ^{12}CO(2-1) highlight the Outer Arm slightly better, Fig. A.1 in Appendix A.1 shows the spectral profile for ALMA.

To aid the comparison between the proposed SW-region and the cluster core, Fig. 4.1 is arranged roughly by longitude (RA), starting with the four SW targets (DFK 68, 5, 1 and 49) at the top. It can then be observed that within the cluster velocity window ($90 - 115$ km/s), the SW sources display a broader and more continuous emission profile that roughly spans over this velocity range. Whereas the remaining sources exhibit narrower line profiles that in some cases are split into distinct double peaks. More specifically, the sources that are not located in the SW seem to trace a second peak at $\sim$ 112 km/s. Furthermore, the overall line intensities are also systematically higher across the SW region compared to the rest of the cluster (Table A.1 in Appendix A.2 present the calculated mean intensities over the full spectral range of -35 to 125 km/s). A notable exception to both trends is DFK 23 which exhibits both a broad spectral profile within the cluster velocity window and exceptionally high overall line intensities despite not being located in the SW region. As seen in Fig. 1.2, DFK 23 is located neither within the SW region nor near the cluster core, but rather a bit more at the edge of the cluster. A plausible reason for this is discussed in Section 5.3.

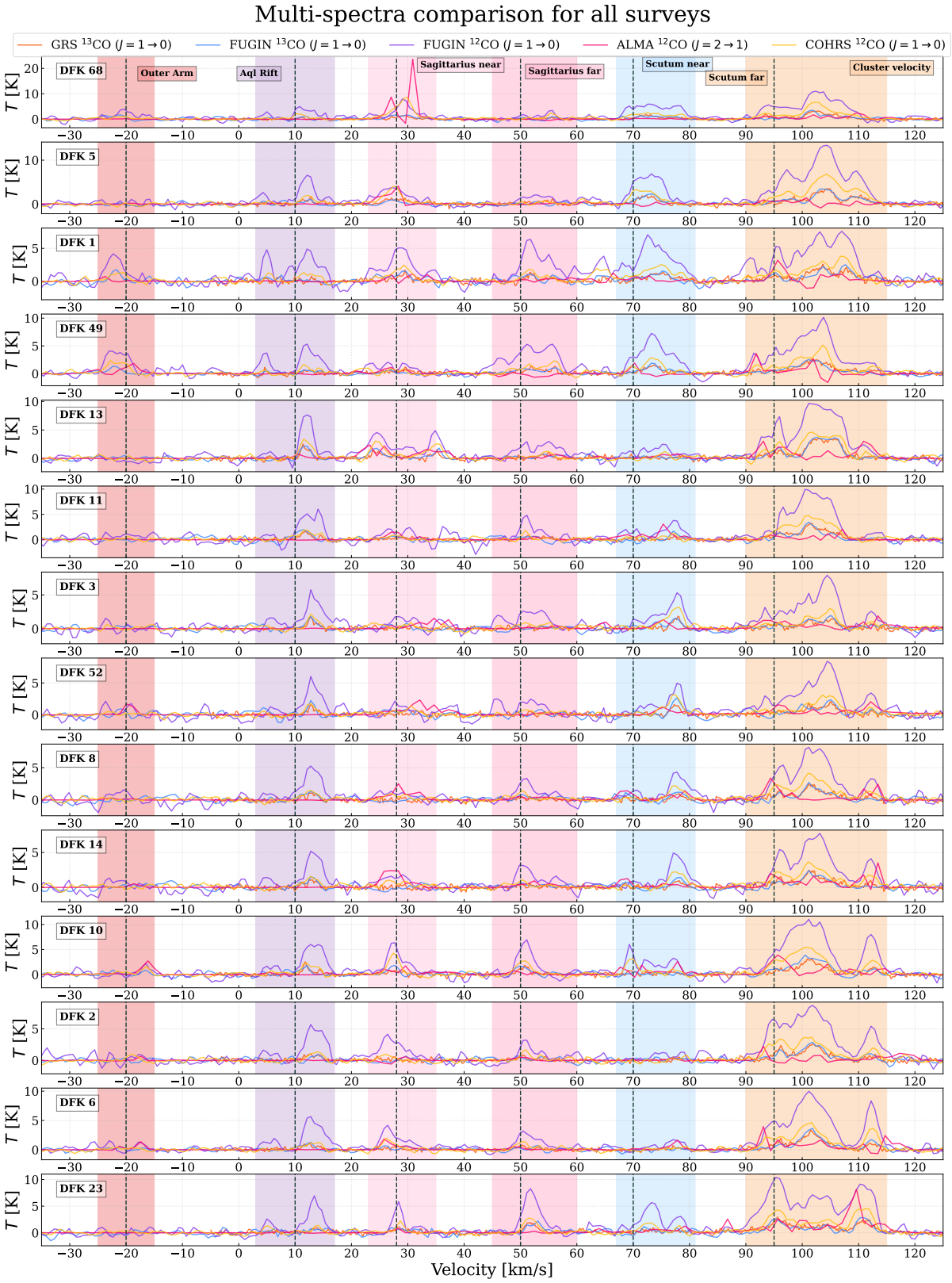


Fig. 4.1: The extracted spectral line profiles across five molecular surveys for each source. The velocity range for each spiral arm is highlighted in different colors and the dotted black line represent the value that was initially extracted from the figure in Dame et al. [29] and Reid et al. [12]. For display clarity, the ALMA ^{12}CO(2-1) line intensities have been scaled by a factor of five.

4.2 The Galactic Spiral Arms

By exploring the moment 0 maps over the velocity ranges for each spiral arm, the molecular structures associated with each intersecting arm can be systematically evaluated. Fig. 4.2 through 4.5 present the moment 0 maps extracted from the four surveys: FUGIN ^{12}CO(1-0), COHRS ^{13}CO(3-2), GRS ^{13}CO(1-0), and FUGIN ^{13}CO(1-0). Each figure displays the integrated intensity for each spiral arm over the respective velocity window, with the exception of the Outer Arm and the far side of the Scutum Crux Arm. Their moment 0 maps can instead be found in Appendix A.3 and Section 4.3, respectively.

Generally, all surveys reveal consistent molecular gas features within each respective velocity window. The primary variations manifest in the integrated emission values (K km/s), where the FUGIN ^{12}CO(1-0) maps exhibit the highest overall integrated intensities, and the GRS ^{13}CO(1-0) maps trace the lowest values. Additionally, the GRS ^{13}CO(1-0) maps depict more extended molecular structures in each velocity window, whereas the FUGIN ^{13}CO(1-0) maps show smaller and more compact molecular structures. These variances reflect their differences in angular resolution, as listed in Table 3.1 and indicated by the beam sizes shown in each figure.

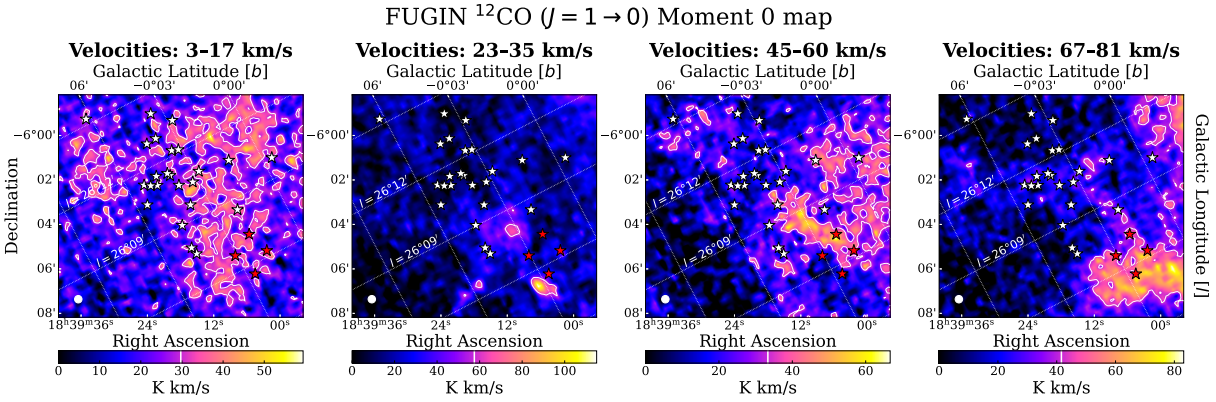


Fig. 4.2: FUGIN ^{12}CO ($J = 1 \rightarrow 0$) moment 0 maps integrated over the spiral arm velocity ranges. White and red stellar symbols mark the cluster core and the SW members, respectively.

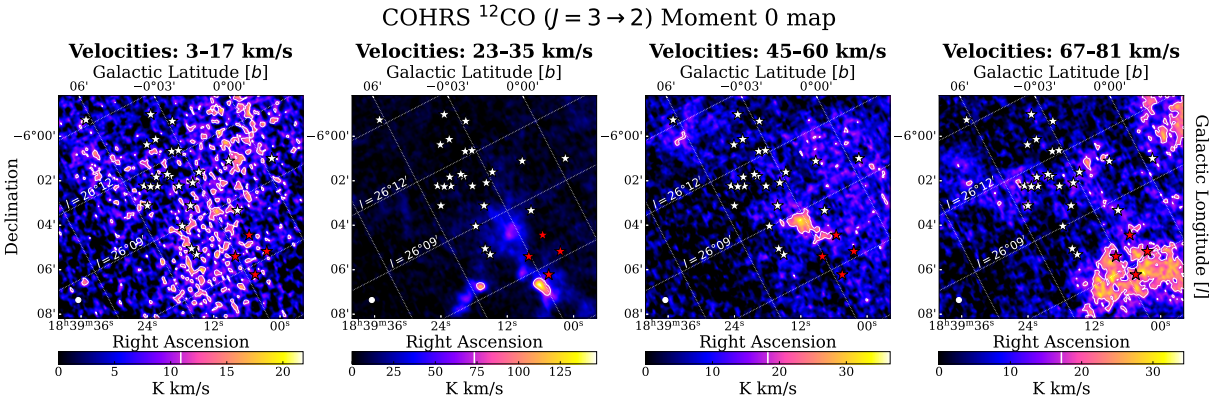


Fig. 4.3: COHRS ^{13}CO ($J = 3 \rightarrow 2$) moment 0 maps integrated over the spiral arm velocity ranges. White and red stellar symbols mark the cluster core and the SW members, respectively.

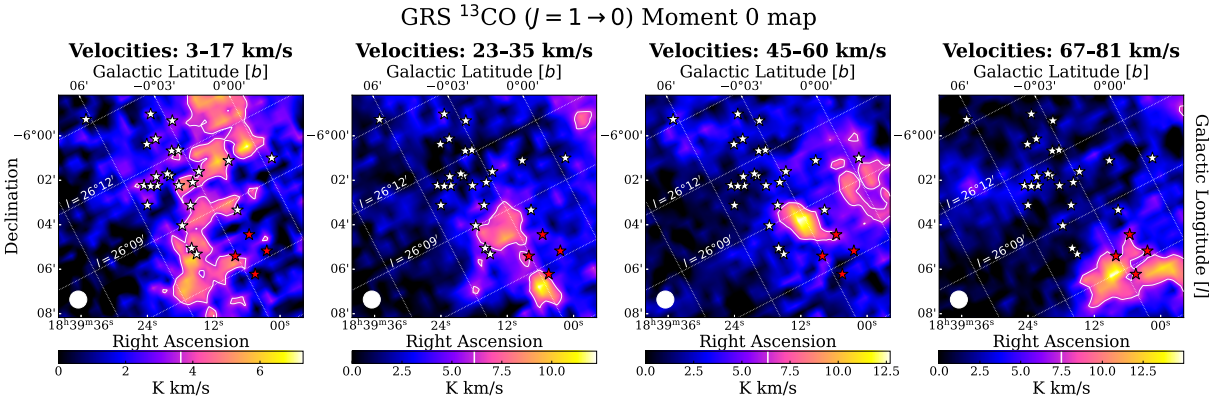


Fig. 4.4: GRS ^{13}CO ($J = 1 \rightarrow 0$) moment 0 maps integrated over the spiral arm velocity ranges. White and red stellar symbols mark the cluster core and the SW members, respectively.

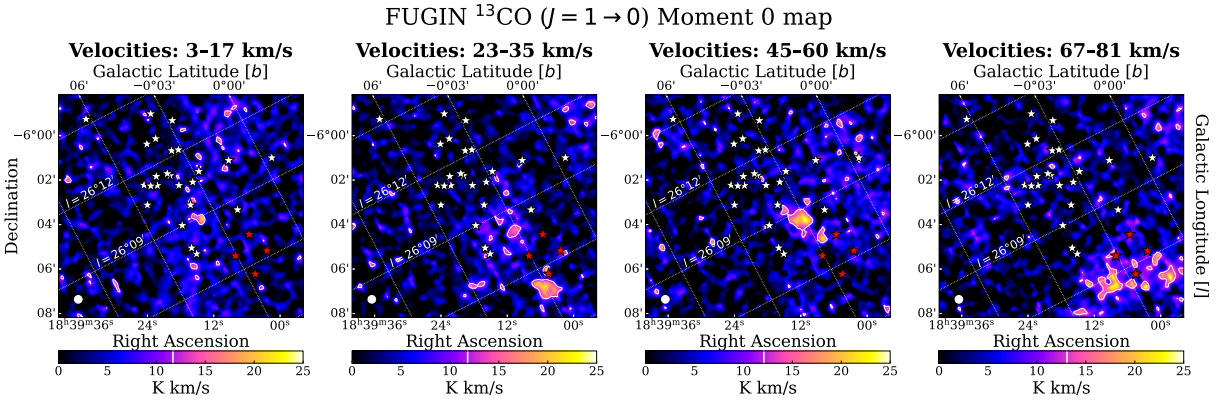


Fig. 4.5: FUGIN ^{13}CO ($J = 1 \rightarrow 0$) moment 0 maps integrated over the spiral arm velocity ranges. White and red stellar symbols mark the cluster core and the SW members, respectively.

4.2.1 The Sagittarius Arm, IRAS 18364-0605, PACS-A and PACS-B.

From the moment 0 maps, the molecular gas structures extracted from the near side of the Sagittarius Arm appear to align with several mid- and far-infrared features identified in the RGB image (Fig. 1.2), specifically, IRAS 18364-0605, PACS-A and PACS-B. To investigate this correlation, Fig. 4.6 and 4.7 display a sequence of nine consecutive velocity channel maps spanning 23.2 to 33.4 km/s. In these figures, the molecular line emission is overlaid as contours on the underlying RGB image, progressing from lower intensity boundaries in yellow to higher intensities in magenta and white. All four surveys map similar and consistent features across this range. However, the emission from ^{13}CO in this velocity window ($23 - 35$ km/s) is very faint as ^{13}CO is less abundant than ^{12}CO and thus less sensitive to diffuse gas. The FUGIN ^{13}CO(1-0) and GRS ^{13}CO(1-0) surveys are therefore excluded from this section. Their respective channel maps can be found in Appendix A.4.

Both figures capture the full channel sequences in which the gas structure emerges at 23.2 km/s and dissipates by 33.4 km/s. Across the first four velocity channels (23.2 – 27 km/s), the molecular emission tightly traces the infrared source, PACS-B in both surveys. Similarly, the envelope of PACS-A also shows spatial correlation, with contours present across the majority of the velocity slices, specifically from 25.8 to 30.9 km/s. Finally, the molecular emission also exhibits a spatial alignment with IRAS 18364-0605. This is particularly pronounced in the

FUGIN ^{12}CO(1-0) map at v = 28.3 km/s, where the molecular gas contours trace the arc geometry of the infrared source.

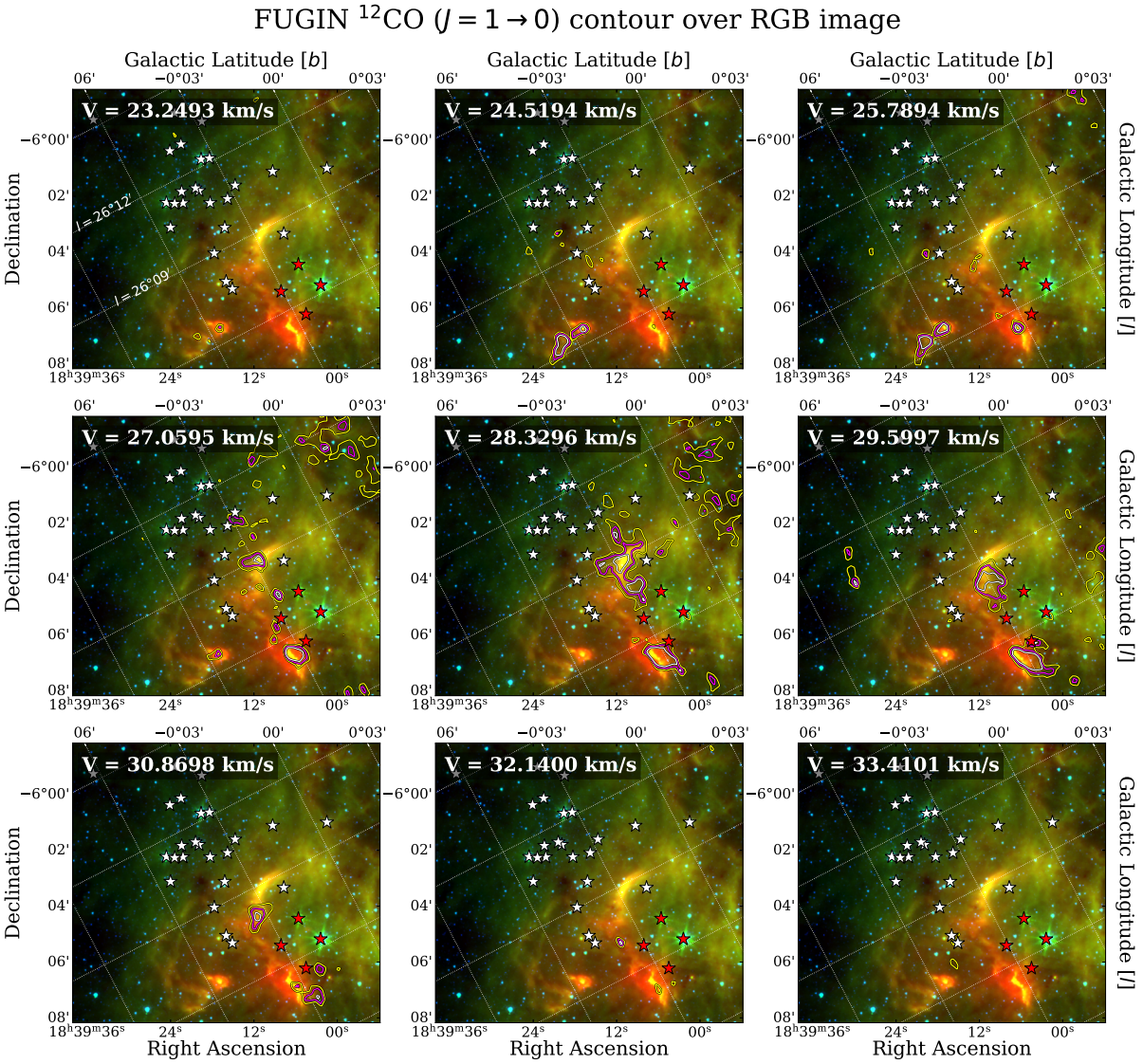


Fig. 4.6: FUGIN ^{12}CO ($J = 1 \rightarrow 0$)velocity channel maps across the Sagittarius Arm (24.5 – 33.4 km/s) overlaid on an RGB image. The emission is represented by contours at temperature levels of 7 K (yellow), 9 K (magenta) and 11 K (white).

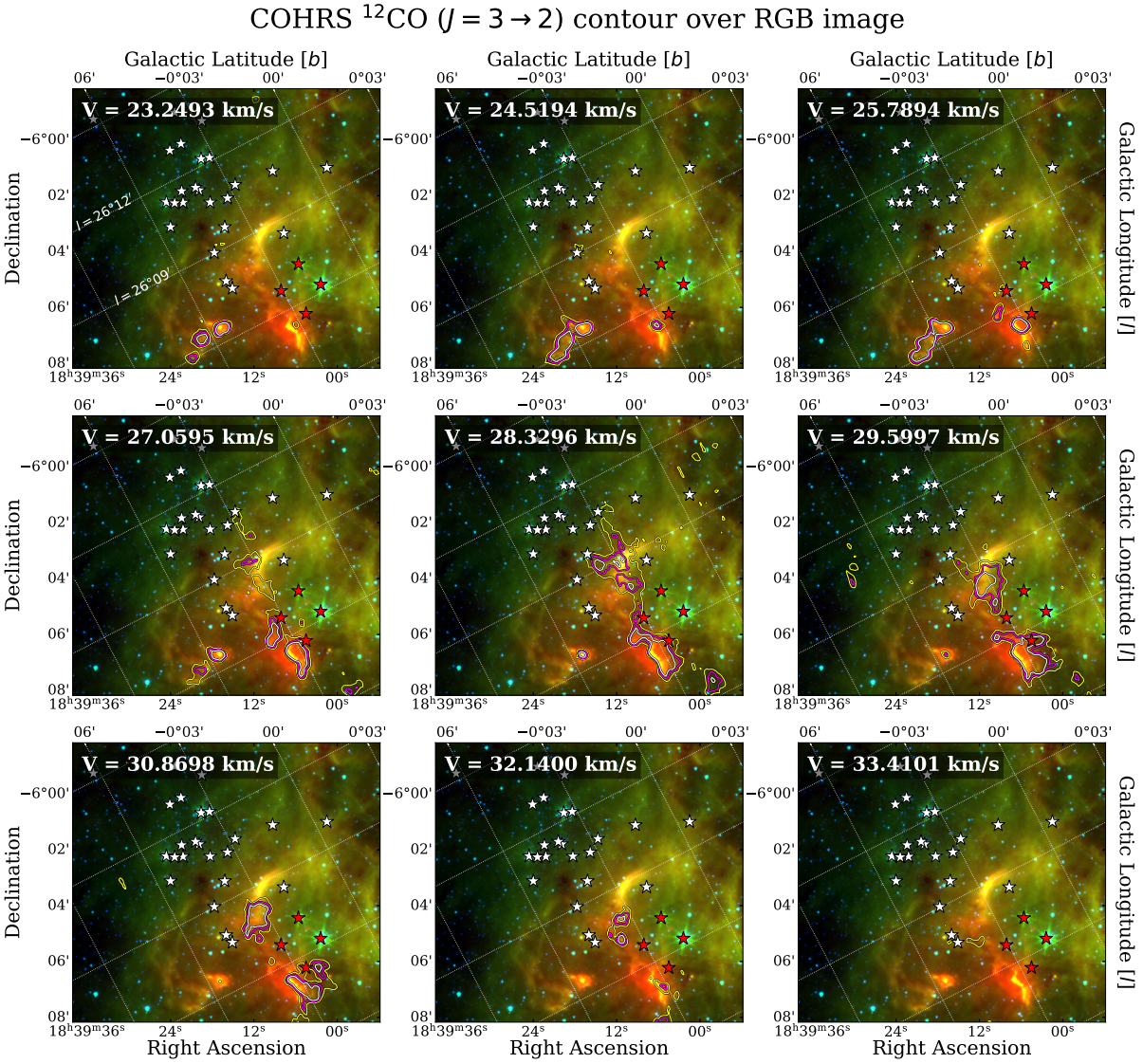


Fig. 4.7: COHRS ^{12}CO ($J = 3 \rightarrow 2$) velocity channel maps across the Sagittarius Arm (24.5 – 33.4 km/s) overlaid on an RGB image. The emission is represented by contours at temperature levels of 4.5 K (yellow), 6.5 K (magenta) and 8.5 K (white).

4.3 At Cluster Velocities

As RSGC2 is situated within the Scutum-Crux Arm, the native cluster velocity range (90 - 115 km/s) captures ISM material associated with both the cluster and this Galactic arm. The moment 0 maps for this velocity window are presented in Fig. 4.8, where each panel displays the integrated intensity map over the cluster velocity for each survey, ordered from left to right: FUGIN ^{12}CO(1-0), COHRS ^{12}CO(3-2), FUGIN ^{13}CO(1-0) and GRS ^{13}CO(1-0). All four maps reveal consistent and similar molecular structures, with small deviations which arise because of differences in angular resolution and the specific molecular tracer used. The structure that is most notably appearing across the integrated intensity map for all surveys is the dense arrangement of gas that extends diagonally before curving upward at the base of the SW region. This forms a distinct molecular barrier that segregates the primary cluster core (white stars) from the SW cluster (red stars). Furthermore, the maps also depict a depletion of molecular gas close to the cluster members, revealing holes of emission around the sources.

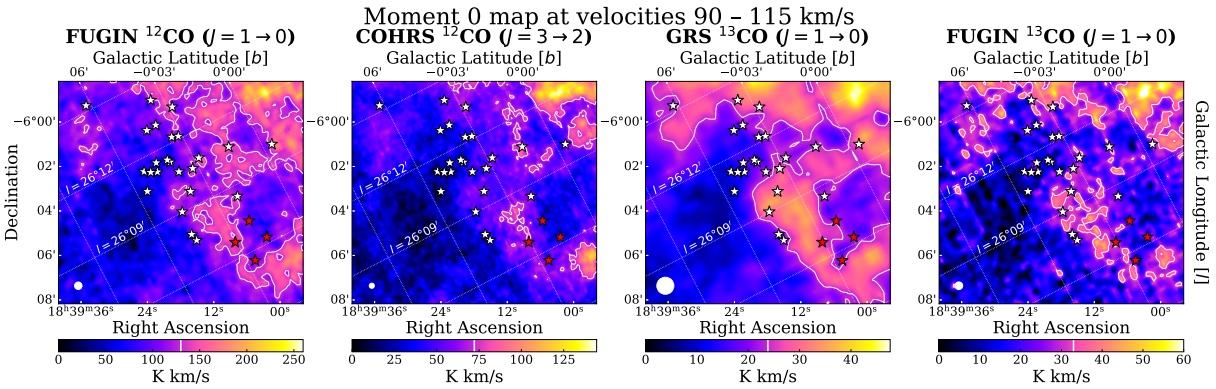


Fig. 4.8: Moment 0 maps at the native cluster velocities range across four surveys, FUGIN ^{12}CO(1-0), COHRS ^{13}CO(3-2), FUGIN ^{13}CO(1-0) and the GRS ^{13}CO(1-0). White and red stellar symbols mark the cluster core and the SW members, respectively.

To provide a more comparable view of the emission across the sources, Table 4.1 presents the mean brightness temperatures calculated over the cluster velocity range ($90 - 115$ km/s) which gives an indication of the cluster ISM. Each row corresponds to a DFK source and its mean emission for each survey. The values indicate that FUGIN ^{12}CO(1-0) exhibits the highest mean brightness temperatures while ALMA ^{12}CO(2-1) records the lowest values. Looking at the FUGIN ^{12}CO(1-0) survey, the five DFK sources with the highest overall intensities are DFK 5, 23, 10, 6 and 68.

Table 4.1: Average brightness temperatures for each DFK source with the respective survey in each column. Note that the unit for all averages are in Kelvin.

DFK	**FUGIN** ^{12}CO(1-0)	**COHRS** ^{12}CO(3-2)	**GRS** ^{13}CO(1-0)	**FUGIN** ^{13}CO(1-0)	**ALMA** ^{12}CO(2-1)
1	3.784 ± 0.111	1.446 ± 0.041	0.838 ± 0.023	0.791 ± 0.046	$0.111 \pm 2.2 \cdot 10^{-3}$
2	4.222 ± 0.055	1.669 ± 0.043	0.784 ± 0.021	0.822 ± 0.049	$0.060 \pm 1.2 \cdot 10^{-3}$
3	2.672 ± 0.074	0.856 ± 0.026	0.481 ± 0.023	0.571 ± 0.053	$0.118 \pm 3 \cdot 10^{-4}$
5	5.475 ± 0.065	2.596 ± 0.040	1.060 ± 0.017	1.099 ± 0.032	$0.071 \pm 1.1 \cdot 10^{-3}$
6	4.348 ± 0.097	1.818 ± 0.023	0.894 ± 0.016	0.931 ± 0.035	$0.167 \pm 4 \cdot 10^{-4}$
8	3.199 ± 0.083	1.492 ± 0.024	0.696 ± 0.034	0.579 ± 0.055	$0.142 \pm 4 \cdot 10^{-4}$
10	4.875 ± 0.102	2.191 ± 0.019	0.876 ± 0.018	1.143 ± 0.035	$0.194 \pm 3 \cdot 10^{-4}$
11	3.597 ± 0.124	1.745 ± 0.051	0.896 ± 0.019	0.764 ± 0.066	$0.078 \pm 2 \cdot 10^{-4}$
13	4.339 ± 0.031	1.861 ± 0.049	1.189 ± 0.021	1.177 ± 0.019	$0.204 \pm 2 \cdot 10^{-4}$
14	3.053 ± 0.065	1.377 ± 0.036	0.696 ± 0.034	0.548 ± 0.049	$0.164 \pm 3 \cdot 10^{-4}$
23	5.780 ± 0.085	2.209 ± 0.054	1.162 ± 0.026	0.999 ± 0.039	$0.369 \pm 3 \cdot 10^{-4}$
49	3.846 ± 0.111	1.579 ± 0.065	0.869 ± 0.023	0.773 ± 0.036	$0.122 \pm 1.6 \cdot 10^{-3}$
52	2.931 ± 0.142	1.009 ± 0.040	0.550 ± 0.026	0.667 ± 0.062	$0.126 \pm 3 \cdot 10^{-4}$
68	4.502 ± 0.198	2.108 ± 0.041	0.922 ± 0.026	0.786 ± 0.056	$0.147 \pm 3 \cdot 10^{-4}$

While Fig. 4.8 reveals a barrier structure between the core cluster and SW sources, Fig. 4.9 provides an additional perspective. By examining the correlation between these moment maps and the cold dust continuum traced by the Herschel PACS160, the physical nature of the identified structures can be further assessed. Although the multi-wavelength RGB image provides a helpful combination of varying thermal phases, isolating the 160 µm emission is beneficial as it selectively traces the most significant concentrations of cold and dense interstellar dust. Fig. 4.9 displays the moment 0 contours for $90 - 115$ km/s from each molecular line survey overlaid directly onto the PACS160 dust emission map. Generally, the moment maps trace the dust emission structures well. As this map extends to a wide-field view of the cluster, more of the molecular gas structure is revealed. Now the molecular barrier is seen to actively circle around the SW stellar population. Moreover, the highest brightness temperatures are detected north of DFK 23 and 31, coinciding with a peak in the PACS160 dust emission.

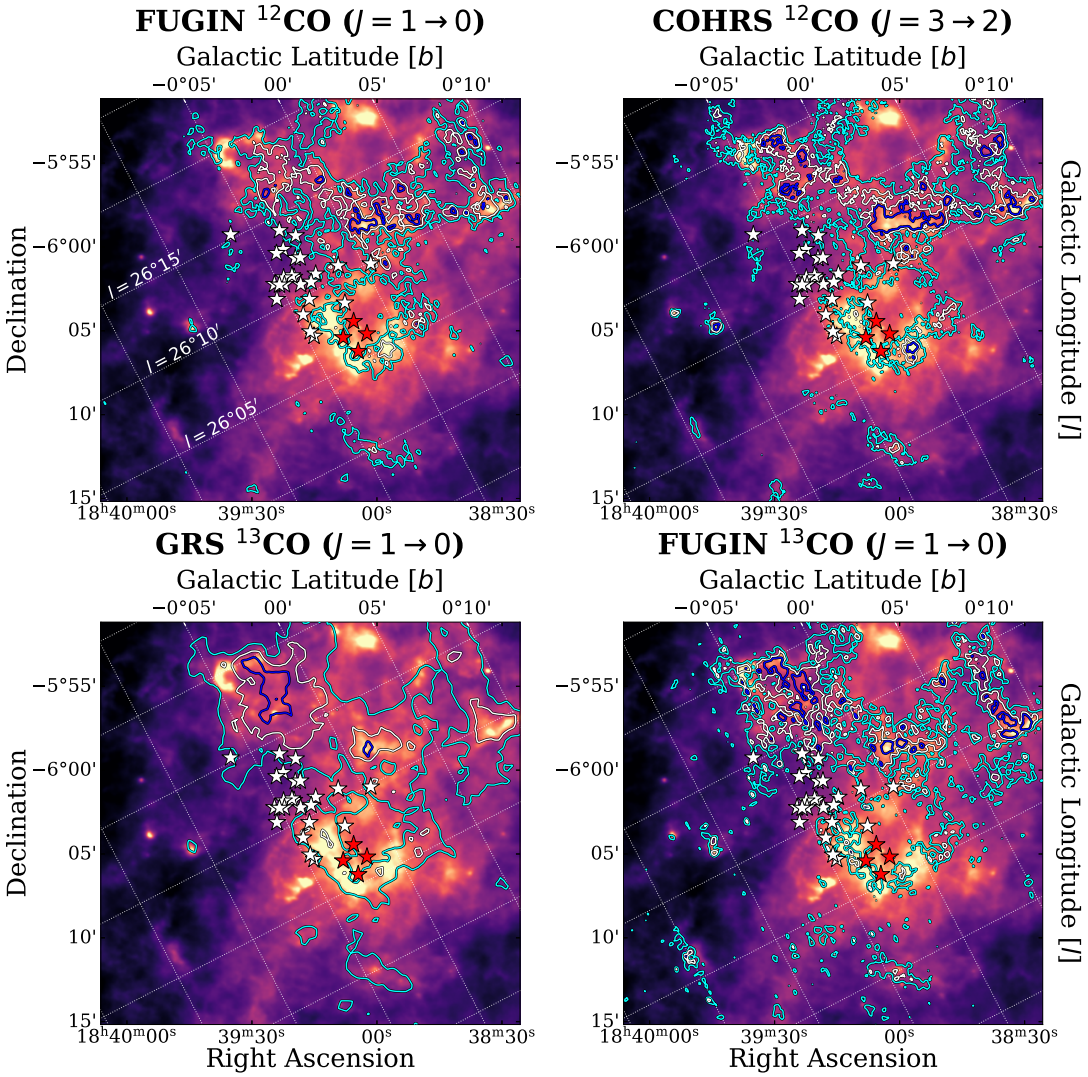


Fig. 4.9: Herschel PACS 160µm far-infrared dust map overlaid with moment 0 contours from the cluster velocity (90-115 km/s). The contour levels for each survey are presented in cyan, white and dark blue with the respective values, FUGIN ^{12}CO(1-0): 130, 160, 190 K km/s, COHRS ^{12}CO(3-2): 10, 20, 30 K km/s, GRS ^{13}CO(1-0): 25, 35, 45 K km/s, FUGIN ^{13}CO(1-0): 30, 40, 50 K km/s

4.3.1 The SW barrier and the infrared sources

From the two-dimensional distribution provided by the moment 0 maps (Fig 4.8 and 4.9), numerous structures can be identified across the cluster region. To move beyond this two-dimensional projection and study the three-dimensional layout of the cluster, it is valuable to examine individual channel maps and track the gas emission across discrete velocity slices. Fig. 4.10 through 4.13 present a sequence of twelve consecutive velocity channel maps spanning from 95.7 to 109.6 km/s. In each figure, the molecular line emission from the respective survey is overlaid as contour lines progressing from blue to purple to magenta. These figures display the wide-field view of the cluster for each of the surveys: FUGIN ^{12}CO(1-0), COHRS ^{12}CO(3-2), GRS ^{13}CO(1-0) and FUGIN ^{13}CO(1-0), respectively.

Using this perspective, several embedded infrared sources alongside the SW barrier can be cleanly isolated and traced as the emission evolves through the velocity windows. The molecular barrier previously identified in the integrated maps (Fig 4.8 and 4.9) is clearly visible in the $v = 102$ km/s channel across all surveys, and can be further distinguished at 100.7 and 103.3 km/s. At these velocities, the barrier does not fully encircle the RSGs in the SW region but instead exhibits a slight curve near the base of the SW region. Furthermore, the barrier spatially overlaps with two infrared sources, IRAS 18364-0605 and PACS-A, which lie directly along the barrier's extent. Another source traced by the gas emission is the supernovae remnant candidate, IRAS 18369-0557, which is most prominently seen in the $v = 99.5$ km/s and 100.7 km/s channels. It is also noted that the emission map for the COHRS ^{12}CO(3-2) survey exhibits a sharp, linear discontinuity along the exact longitude of $l = 26°15'$. This artifact comes from an edge effect which arises from the combination of two adjacent tiles in the wide-field mosaic.

Lastly, just as Table 4.1 outlines the mean brightness temperature for each DFK source, the same methods are applied to compute the mean temperatures for the infrared sources. This is presented in Table 4.2. The IRAS and PACS sources exhibit in general a higher line intensity than the DFK sources, with the exception of PACS-B who seem to have lower averaged line intensities than the DFK sources.

Table 4.2: Average brightness temperatures over the velocity range of 90-115 km/s for each survey. Note that the unit for all intensity averages are in Kelvin.

Source	**FUGIN** ^{12}CO(1-0)	**COHRS** ^{12}CO(3-2)	**GRS** ^{13}CO(1-0)	**FUGIN** ^{13}CO(1-0)
IRAS 18369-0557	4.645 ± 0.027	2.699 ± 0.017	1.309 ± 0.010	1.420 ± 0.022
IRAS 18367-0556	4.674 ± 0.047	1.978 ± 0.025	1.224 ± 0.017	1.121 ± 0.041
IRAS 18364-0605	5.048 ± 0.024	2.418 ± 0.015	1.050 ± 0.013	1.056 ± 0.013
PACS-A	4.944 ± 0.057	2.269 ± 0.026	1.070 ± 0.012	0.973 ± 0.024
PACS-B	3.157 ± 0.050	1.084 ± 0.024	0.610 ± 0.015	0.685 ± 0.016

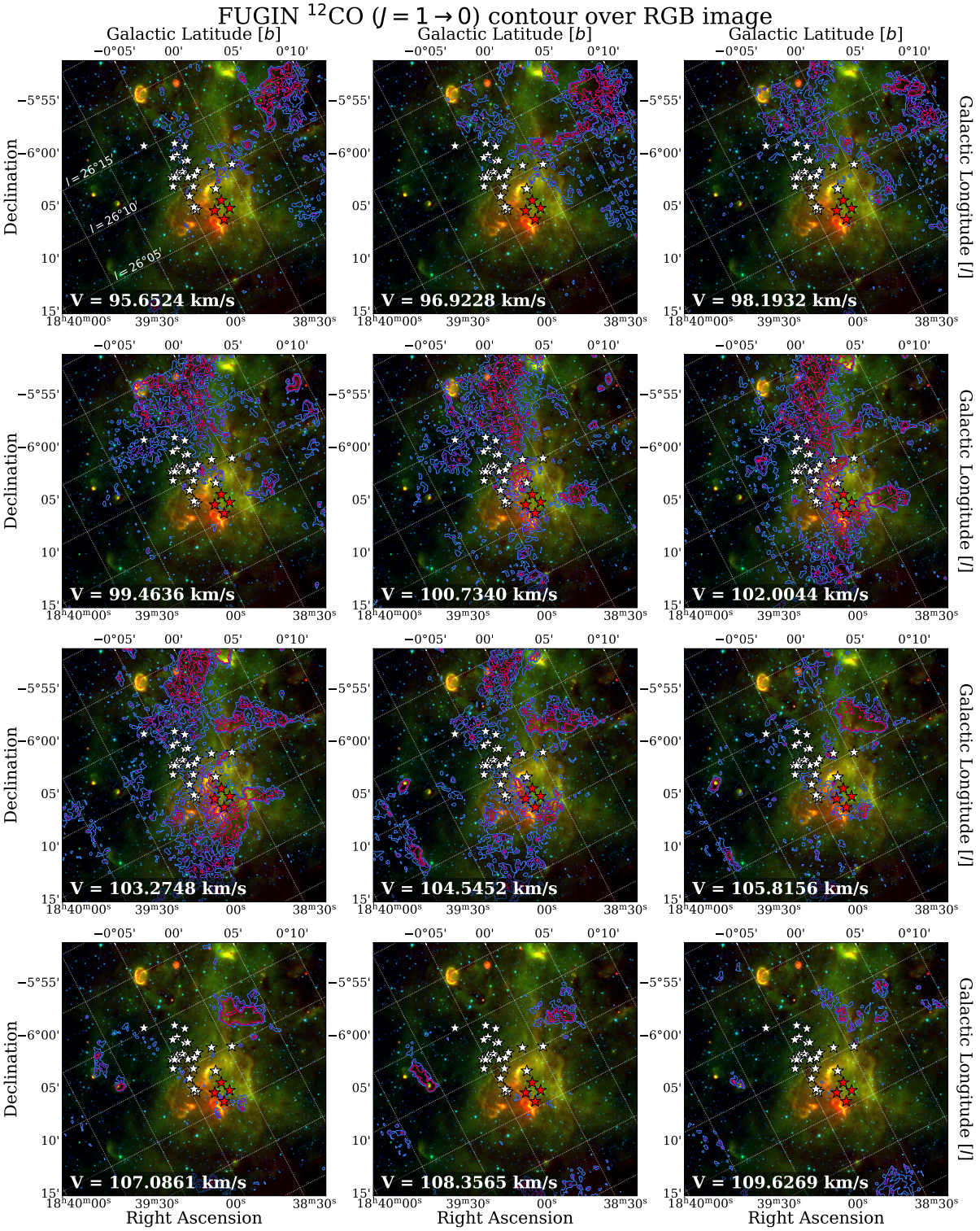


Fig. 4.10: FUGIN ^{12}CO ($J = 1 \rightarrow 0$) velocity channel across the velocity window, 95.7 to 109.6 km/s, overlaid on an RGB image. The emission is represented as contours at temperature levels of 9 K (blue), 11 K (purple) and 13 K (magenta).

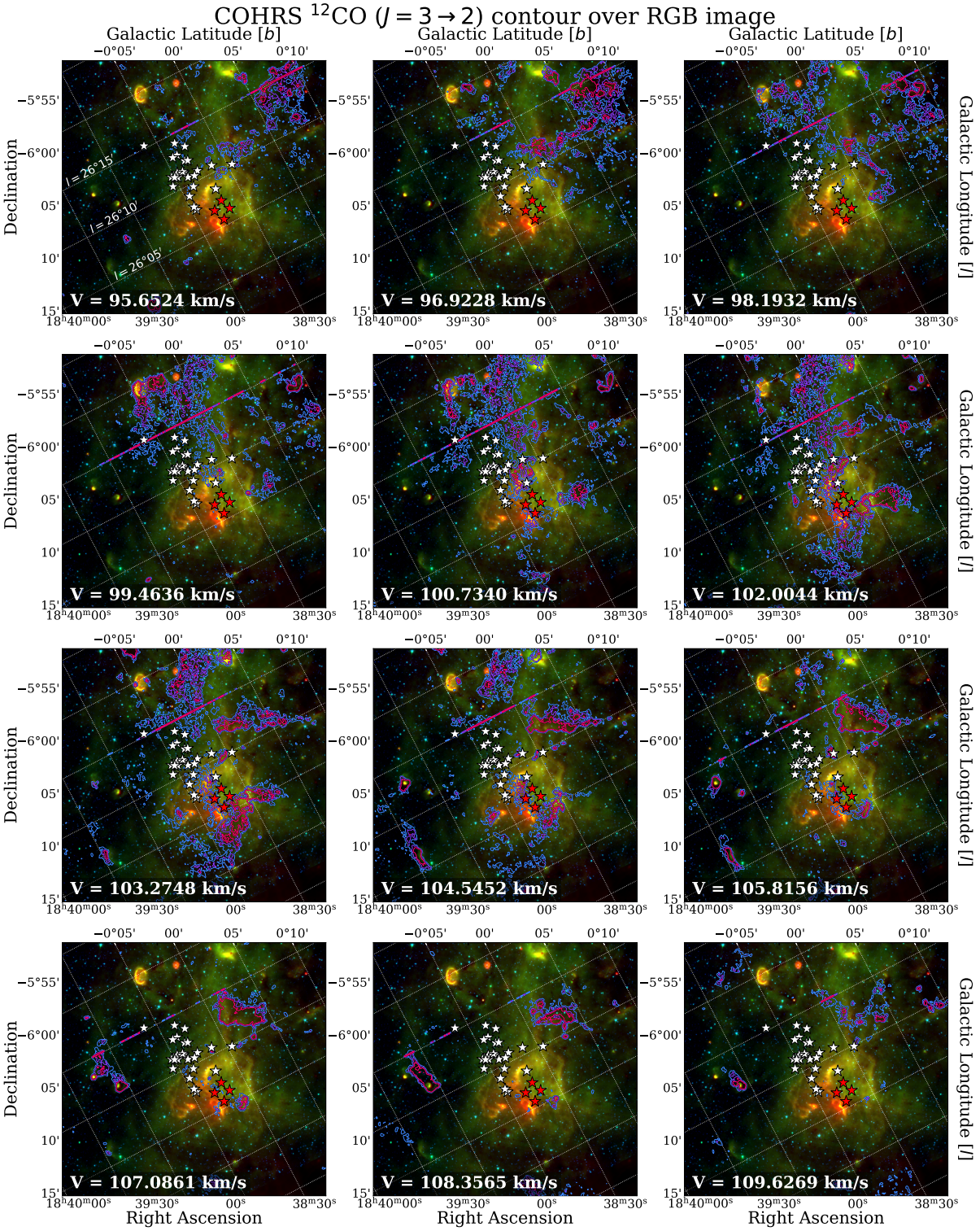


Fig. 4.11: COHRS ^{13}CO $J = 3 \rightarrow 2$ velocity channel across the velocity window, 95.7 to 109.6 km/s, overlaid on an RGB image. The emission is represented as contours at temperature levels of 5 K (blue), 6.5 K (purple) and 8 K (magenta)

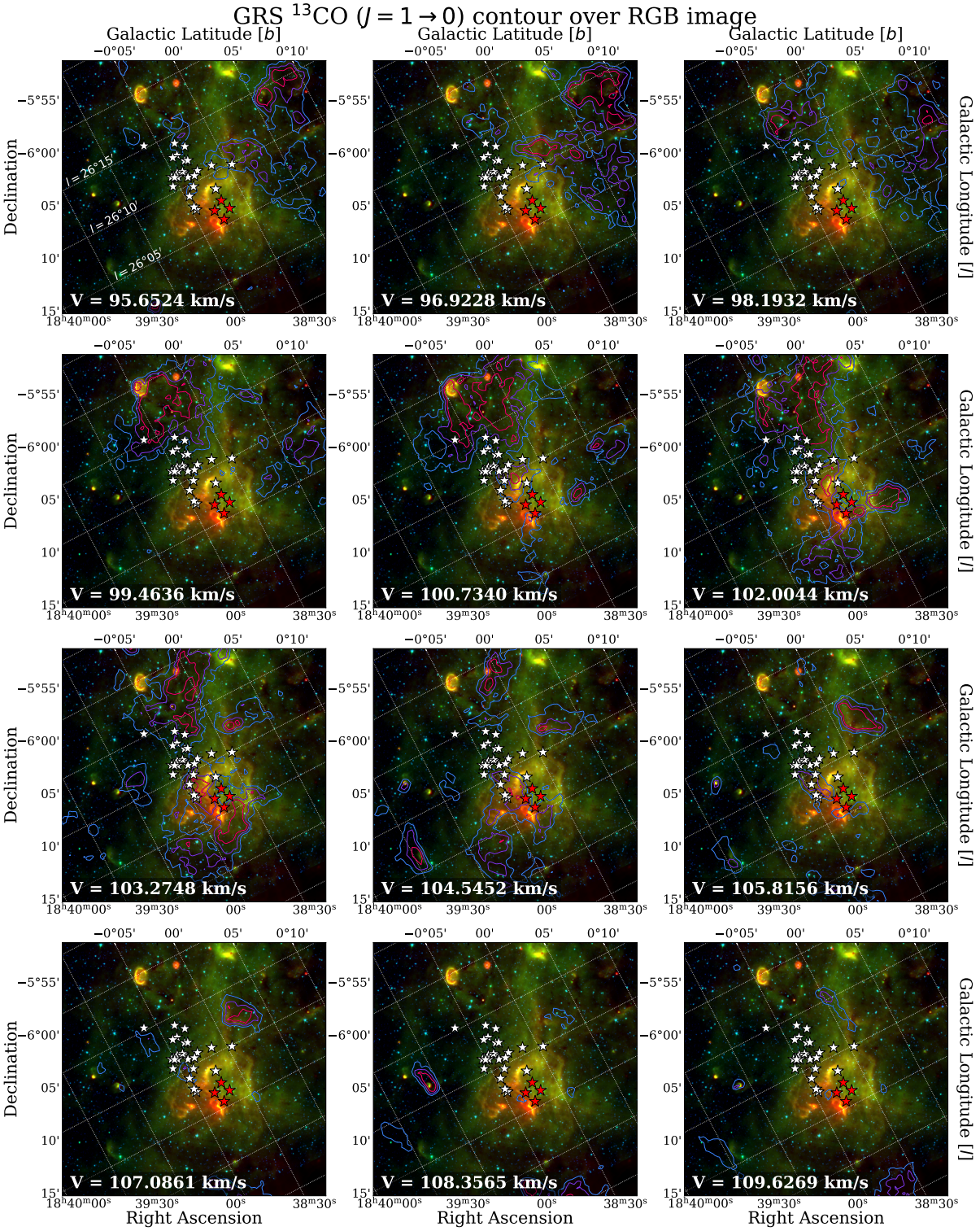


Fig. 4.12: GRS ^{13}CO $J = 1 \rightarrow 0$ velocity channel across the velocity window, 95.7 to 109.6 km/s, overlaid on an RGB image. The emission is represented as contours at temperature levels of 2 K (blue), 3 K (purple) and 4 K (magenta).

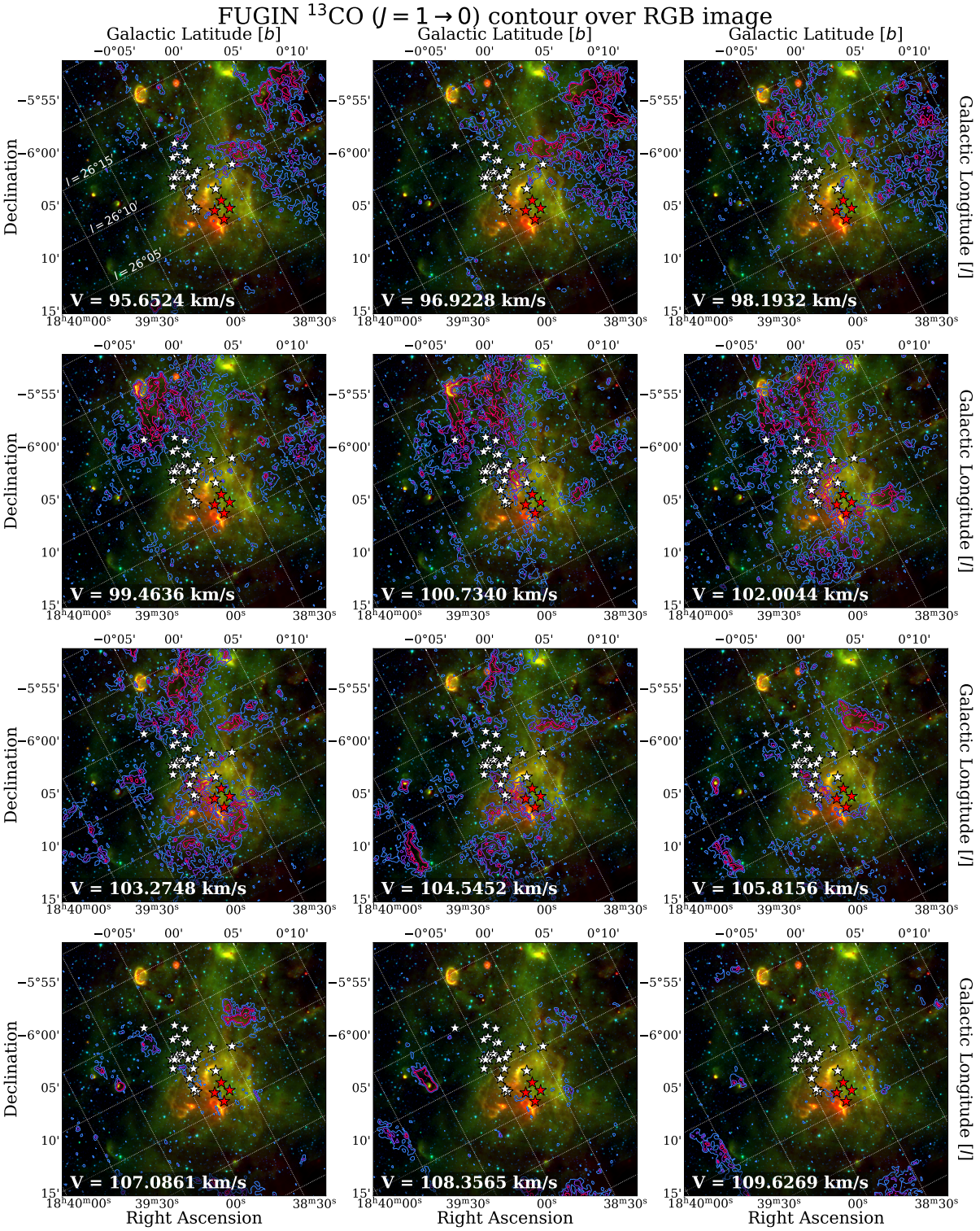


Fig. 4.13: FUGIN ^{13}CO $J = 1 \rightarrow 0$ velocity channel across the velocity window, 95.7 to 109.6 km/s, overlaid on an RGB image. The emission is represented as contours at temperature levels of 2.5 K (blue), 3.25 K (purple) and 4K (magenta).

4.4 CO Line Ratios

The molecular line emission ratios were computed for each source over the cluster velocity window and presented in Tab 4.3 (See Eq. (3.1) for the ratio definitions). Each ratio is calculated for the various DFK sources and the overall average ratio is $R_{(3-2)/(1-0)} = 0.418 \pm 0.004$, and $R_{12/13} = 4.864 \pm 0.089$. According to Peñaloza et al. [33], the ratio for Galactic massive clusters is $R_{(3-2)/(1-0)} = 0.5 \pm 0.2$, where large error margin arises from the difference in excitation conditions for both lines. The value found here lies within this margin.

For $R_{12/13}$, no specific value for RSGC2 could be found. However, the Galactic center has a value of ~ 20 and as RSGC2 is located near the base of the Scutum-Crux arm, close to the Galactic center, the expected value should be around 20. The results shows a much lower value than 20, suggesting that the ^{12}CO emission toward these sources is highly optically thick.

The ratios can also be computed over the whole spectral range (-35 – 125 km/s), which yield the mean values, $R_{(3-2)/(1-0)} = 0.389 \pm 0.004$ and $R_{12/13} = 4.383 \pm 0.078$. (See Table A.3 for all ratios). For comparison, Park et al. [25] calculated the $R_{(3-2)/(1-0)}$ ratio over a longitude of $10° \geq l \geq 50°$ and a latitude of $|b| \leq 5°$, finding a mean value of $R_{(3-2)/(1-0)} = 0.27$. However, as this represents an average over the full latitude range, it is not directly comparable to the value found here. A more representative estimate can instead be extracted from figure 12 by Park et al. [25], from which the ratio at RSGC2's given longitude ($l \approx 26°$) can be approximated as $R_{(3-2=/(1-0)} \approx 0.35$.

Table 4.3: Line intensity ratios for the observed DFK sources over the velocity range of 90 – 115 km/s. The overall sample average for $R_{(3-2)/(1-0)} = 0.418 \pm 0.004$, and for $R_{12/13} = 4.864 \pm 0.089$.

Source	$R_{(3-2)/(1-0)}$	$R_{12/13}$
1	0.382 ± 0.016	4.782 ± 0.310
2	0.395 ± 0.011	5.135 ± 0.311
3	0.320 ± 0.013	4.679 ± 0.451
5	0.474 ± 0.009	4.986 ± 0.157
6	0.418 ± 0.011	4.670 ± 0.207
8	0.466 ± 0.014	5.526 ± 0.541
10	0.449 ± 0.010	4.266 ± 0.159
11	0.485 ± 0.022	4.711 ± 0.441
13	0.429 ± 0.012	3.687 ± 0.065
14	0.451 ± 0.015	5.572 ± 0.514
23	0.382 ± 0.011	5.786 ± 0.242
49	0.411 ± 0.021	4.974 ± 0.274
52	0.344 ± 0.022	4.407 ± 0.459
68	0.468 ± 0.023	5.726 ± 0.479

Finally, the ratios for the infrared sources are presented in Table 4.4 and 4.5, computed over the velocity range of the cluster and the Sagittarius Arm respectively. This allows a numerical comparison of the ratios to aid the discussion regarding the association of some of the infrared features. The ratios for the infrared sources over the whole spectral window can also be found in Table A.4 in Appendix A.5. The most notable difference between the two velocity windows presented here is the $R_{(3-2)/(1-0)}$ values for PACS-A and PACS-B, which are considerably higher at the Sagittarius Arm velocity than the cluster velocity. IRAS 18369-0557 and IRAS 18367-0556 also show high error uncertainties for $R_{12/13}$.

Table 4.4: Line intensity ratios for the IRAS and PACS sources over the cluster velocity range ($90 - 115$ km/s)

Sources	$R_{(3-2)/(1-0)}$	$R_{12/13}$
IRAS 18369-0557	0.581 ± 0.005	3.272 ± 0.054
IRAS 18367-0556	0.423 ± 0.007	4.169 ± 0.157
IRAS 18364-0605	0.479 ± 0.004	4.778 ± 0.065
PACS-A	0.459 ± 0.008	5.083 ± 0.138
PACS-B	0.343 ± 0.009	4.609 ± 0.129

Table 4.5: Line intensity ratios for the IRAS and PACS sources over the Sagittarius Arm velocity range ($23 - 35$ km/s)

Sources	$R_{(3-2)/(1-0)}$	$R_{12/13}$
IRAS 18369-0557	0.320 ± 0.026	7.184 ± 1.534
IRAS 18367-0556	0.432 ± 0.031	5.858 ± 1.335
IRAS 18364-0605	0.643 ± 0.012	6.059 ± 0.274
PACS-A	1.086 ± 0.028	4.884 ± 0.265
PACS-B	1.024 ± 0.031	4.596 ± 0.218

5

Discussion

This chapter presents a detailed discussion about the implications of the results presented in Chapter 4. Section 5.1 provides a brief overview of the Galactic spiral arm structures identified along the line of sight toward RSGC2. Section 5.2 examines the infrared sources identified in the RSGC2 region including IRAS 18369-0557, IRAS 18367-0556, IRAS 18364-0605, and the four unidentified cold molecular structures, PACS-A, PACS-B, PACS-C and PACS-D. Section 5.3 discusses the evidence for the SW region as a separate cluster alongside the physical nature and implications of the molecular gas barrier. Section 5.4 interprets the molecular line ratio values in the context of the cluster environment. Lastly, Section 5.5 outlines directions for future work.

5.1 The Spiral Arms

The spectral profiles toward the RSGs in RSGC2 over the spectral velocity window of -35 – 125 km/s are displayed in Fig. 4.1. Overall, the profiles show enhanced emission at the expected spiral arm velocities, confirming that they are in the line of sight of RSGC2. A notable exception is the Outer Arm, where emission is mostly detected in the ALMA ^{12}CO(2-1) survey. Given that the Outer Arm is the most distant structure along this line of sight, its emission is intrinsically weak and challenging to detect across all surveys. The detection in ALMA ^{12}CO(2-1) likely reflects a combination of the specific sensitivity and spatial frequency coverage of these observations, though the low brightness temperatures make the detection subtle in the spectra with all surveys. Another observation is the second peak that starts appearing at $\sim$ 112 km/s for most of the sources that are not part of the SW region (DFK 3, 52, 8, 14, 10, 2, 6 and 23). Looking only at the spectral profile, this could indicate a separate molecular structure that is situated behind our sources and molecular barrier. However, inspecting the channel maps around this velocity does not show any significant structures. This peak could instead be an effect from the dynamics of the cluster and how it moves dynamically, with respect to the galactic rotation.

Another way of highlighting the spiral arms is through the moment 0 maps shown in Fig. 4.2 through 4.5. These four figures clearly demonstrate that discrete Galactic spiral arms can be mapped and isolated along the line of sight towards RSGC2. All surveys show consistent molecular features within each velocity window. The largest molecular gas structure appears in the Aquila Rift velocity window ($3 - 17$ km/s), which also corresponds to the overall high emission peaks detected in the spectral profiles for this velocity range. The brightest structures are however seen in the Sagittarius Arm window ($23 - 35$ km/s), where the integrated intensities indicated in the colorbar are generally the highest for this spiral arm across all surveys. Notably, the molecular structures detected in the moment 0 maps for this arm spatially coincide with the infrared sources, IRAS 18364-0605, PACS-A, and PACS-B, suggesting these sources might be associated with the Sagittarius Arm. This will be further discussed in the following sections.

From this, it is possible to confirm that the different foreground spiral arms can be isolated and detected in the line of sight towards RSGC2, with the Outer Arm being slightly more difficult to detect. While these large-scale spiral arm structures provide important context for interpreting the line of sight environments, the most relevant question concerns the association of specific infrared sources with the galactic spiral arms or the cluster itself.

5.2 The Infrared Sources

There are several infrared sources identified within and around the RSGC2 cluster region. Establishing whether these sources are physically associated with the cluster or if they correspond to unrelated foreground structures along the line of sight is critical for correctly interpreting the molecular gas and dust environment of RSGC2.

5.2.1 IRAS 18369-0557

The supernova remnant candidate IRAS 18369-0557 is identified across several figures. Figure 5.1 displays three of the results already presented in Chapter 4 but centered on IRAS 18369-0557 and IRAS 18367-0556, which are also indicated in the Figure.

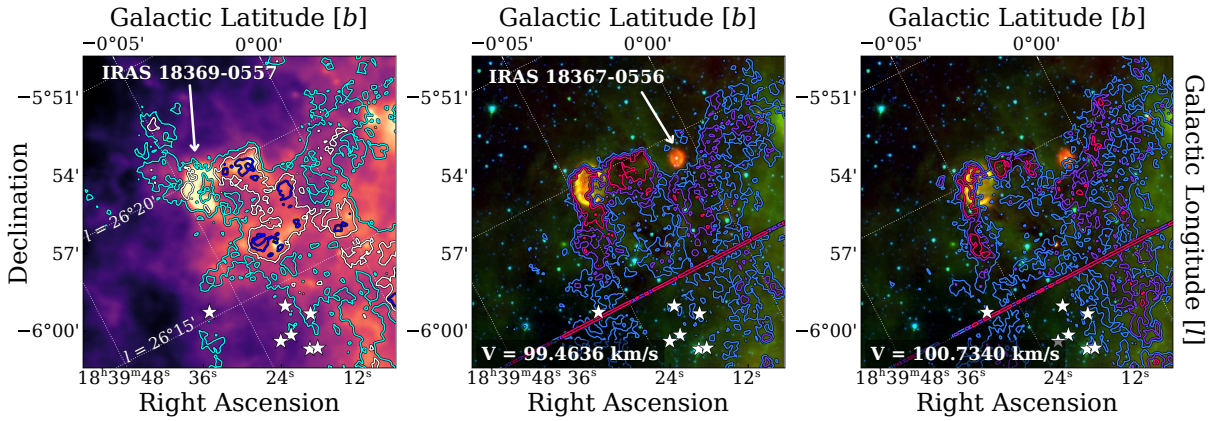


Fig. 5.1: Three plots showing IRAS 18369-0557 and IRAS 18367-0556 with data from COHRS ^{12}CO(3-2) as contours. The first plot displays the moment 0 map over the cluster velocity (90-115 km/s) as contours with the levels 10 (cyan), 20 (white), and 30 (purple) K km/s overlaid on the PACS160 dust emission image. The other two plots show the channel maps as contours overlaid on the RGB image at $v = 99.5$ and $v = 100.7$ km/s, with the levels at 5 K (blue), 6.5 K (purple) and 8 K (magenta).

In the comparative analysis between the RGB image and the Herschel/PACS 160 µm dust continuum map shown in Fig. 1.2 and Fig. 5.1, the source is clearly recovered in both images. The characteristic crescent shaped is traced out, albeit appearing as a more diffuse emission feature in the PACS160 image. The fact that this structure appears in the far-infrared regime suggests a presence of cold dust grains. In addition to this crescent geometry, the PACS160 with the moment 0 map overlaid as contours, does also reveal arc-like structures extending from the two tips of the crescent. This is visible in Fig 4.9 (best seen in the COHRS ^{12}CO(3-2) and FUGIN ^{13}CO(1-0) panels) and the left plot of Fig. 5.1, where regions of substantial gas emission is localized around the perimeter of IRAS 18369-0557. This gas emission appears to trace the crescent shape of the source before extending outward toward the regions of highest intensities.

The crescent-like shape is also clearly resolved in the channel maps over the cluster velocity window (Fig. 4.10 to 4.13), where IRAS 18369-0557 is unambiguously detected in the $v = 99.5$ and $v = 100.7$ km/s channels, more clearly shown in Fig. 5.1. The gas contours accurately follow the shape of the source, and the same outward extending structure discussed above is clearly traced in the same channel maps. This is observed in all surveys, but is somewhat less defined in the FUGIN ^{12}CO(1-0) maps which is consistent with the high optical depth of the ^{12}CO line, causing it to only trace the outer surface of the shell. The optically thinner ^{13}CO lines, however, cleanly trace the shell structure, specifically the eastern side, and its internal boundaries. These kinematic results are further supported by Table 4.4 where IRAS 18369-0557 yields the highest $R_{(3-2)/(1-0)}$ ratio among the infrared targets, indicating warmer and denser gas, consistent with shock-heated material in an expanding shell. Together, these results support the hypothesis that IRAS 18369-0557 is a supernova remnant, characterized by a dense expanding shell with no active central heating engine. Its unambiguous detection at the cluster velocity strongly suggests that the progenitor star was physically associated with RSGC2 prior to the supernova explosion.

5.2.2 IRAS 18367-0556

IRAS 18367-0556 is clearly identified in the RGB image while it is largely absent in the PACS160 image (See Fig 1.2), implying that its emission profile is dominated by warm dust rather than cold dust reservoir. A faint outline may be distinguishable in the PACS160 image, but its extremely weak appearance is consistent with the source being predominantly warm. This feature is also not observed to be specifically traced by any channel map over either the cluster velocity or the Sagittarius Arm velocity windows. However, it is arguable that the emission is instead avoiding this region. Looking at the source in left panel of Fig. 5.1, the integrated intensity seems to bend around it. This lack of molecular gas is also seen in the two channel maps shown in Fig. 5.1, suggesting that the central source may have cleared a cavity in the surrounding cold molecular gas through stellar winds. This, combined with a warm dust dominated profile, supports the earlier interpretation of IRAS 18367-0556 as a highly reddened evolved massive star that shines through a warm envelope.

5.2.3 PACS-A and PACS-B

PACS-A and PACS-B are two far-infrared sources first identified in the RGB image of the RSGC2 region. Figure 5.2 displays two of the central results for these sources already presented in Chapter 4 but now centered on PACS-A, PACS-B and IRAS 18364-0605 which are also indicated in the Figure.

A comparison between the RGB image and the PACS160 dust continuum map reveals distinct dust properties for each of the two sources (See Fig 1.2). PACS-B is clearly recovered across both images, appearing as a slightly extended emission feature in the PACS160 image, indicating a concentration of cold dust surrounding a warmer inner core. PACS-A, on the other hand, is not recovered as a distinct feature in the PACS160 image, with its compact internal structures becoming indistinguishable within the extended cold dust emission. Both features are therefore embedded within a broader molecular cloud environment (even broader for PACS-A) dominated by reservoirs of cold gas and dust.

The kinematic association of both sources is investigated through the channel maps of the Sagittarius Arm velocity window (Fig. 4.6 and 4.7). The molecular gas contours in both FUGIN ^{12}CO(1-0) and COHRS ^{12}CO(3-2) surveys align well with the shape of PACS-A and PACS-B, demonstrating that both sources are associated with a multiphase gas environment containing diffuse cold gas as well as warmer denser material. For PACS-B, the gas contours reveal a more

spatially extended and elongated structure than the compact source visible in the RGB image ($v = 24.5$ to 27.1 km/s). This is however consistent with the more diffuse geometry of PACS-B in the PACS160 image. For PACS-A, the gas contours trace the "lightning bolt" shape seen in the RGB map. This is particularly seen for the COHRS ^{12}CO(3-2) survey ($v = 27.1$ to $v = 30.9$ km/s) or better shown in the left panel of Fig. 5.2, indicating a strong spatial correspondence between the molecular gas and the thermal dust emission of this source.

In contrast, the channel maps across the cluster velocity window can be argued to trace a similar structure of PACS-A. This is best seen in the $v = 102$ km/s channel map where the gas contours follows the shape of PACS-A quite well (right panel in Fig. 5.2). However, the emission manifests as fragmented contour lines that trace only the broad curvature of the feature rather than its distinctive shape. Unlike the cohesive "lightning bolt" geometry that is clearly recovered at the Sagittarius Arm velocity. This argues against a physical association with the cluster environment. Despite this lack of structural tracing, PACS-A still exhibits high average temperatures in the cluster velocity, as seen in Table 4.2 where it generally show high values when tracing ^{12}CO transitions. This is however most likely attributed to the emission of the molecular barrier that dominates this velocity range rather than emission from the sources themselves.

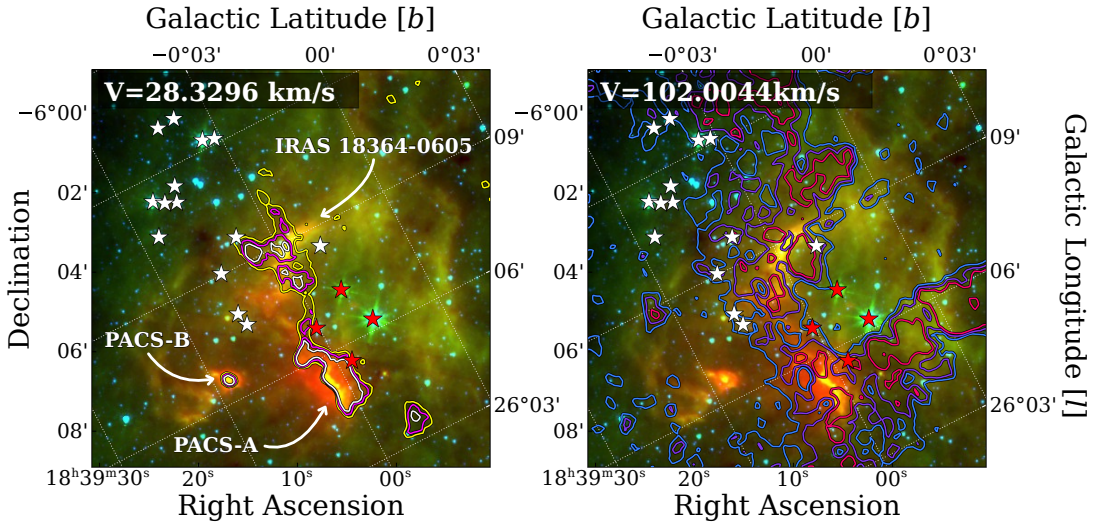


Fig. 5.2: Two channel maps showcasing the three infrared sources, PACS-A, PACS-B and IRAS 18364-0605. The left plot displays the channel map of COHRS ^{12}CO(3-2) as contours at the levels of 4.5 K (yellow), 6.5 K (magenta) and 8.5 K (white) for $v = 28.3$ km/s which is associated with the Sagittarius Arm. The right panel shows the channel map of FUGIN ^{12}CO(1-0) at the levels of 9 K (blue), 11 K (purple) and 13 K (magenta) for $v = 102$ km/s, associated with the cluster velocity.

This interpretation is further supported by the molecular line ratios presented in Table 4.4 and Table 4.5. For both sources, the $R_{(3-2)/(1-0)}$ is significantly higher at the Sagittarius Arm velocity ($R_{(3-2)/(1-0)} = 1.086 \pm 0.028$ and $R_{(3-2)/(1-0)} = 1.024 \pm 0.031$ respectively) compared to the cluster velocity ($R_{(3-2)/(1-0)} = 0.459 \pm 0.008$ and $R_{(3-2)/(1-0)} = 0.343 \pm 0.009$ respectively). As $R_{(3-2)/(1-0)}$ is sensitive to gas temperature and density, higher values indicates warmer and denser excitation conditions. This elevated ratio at the Sagittarius Arm confirms that the gas associated with these sources is more energetically excited which is consistent with the sources being physically embedded in the Sagittarius Arm environment. The $R_{12/13}$ ratio shows no

significant difference between the two velocity ranges. This is expected as this ratio primarily traces optical depth rather than thermal conditions. With these results, PACS-A and PACS-B are most likely physically associated with the Sagittarius Arm rather than the RSGC2 cluster.

5.2.4 IRAS 18364-0605

IRAS 18364-0605, previously identified as a bow shock candidate by Davies et al. [7], resides toward the center of RSGC2, where multiple molecular and dust structures converge along the line of sight (see Fig. 5.2). In the PACS160 dust continuum image, a large extended structure covers the region over both IRAS 18364-0605 and PACS-A, which makes the compact individual components become indistinguishable. As with PACS-A, this behavior indicates that the internal structures are associated with a much warmer dust phase, while the surrounding molecular cloud environment remains dominated by reservoirs of cold gas and dust.

The kinematic profile of this source is more complex than that of PACS-A and PACS-B. There are mainly two velocity ranges in which this infrared source is seen, the Sagittarius Arm and the cluster velocity, both of which are displayed in Fig. 5.2 as channel maps of $v = 28.3$ km/s and $v = 102$ km/s. Fig. 4.6 and Fig. 4.7 display the channel maps over the velocity range for the Sagittarius Arm, where the gas contours trace the infrared boundaries of the source, suggesting a possible physical association. However, this correlation is only clearly seen across a narrow velocity window (28.3 and 29.6 km/s) while for PACS-A and PACS-B, the correlation is seen in several consecutive channel maps. Furthermore, the gas contours at these channel maps trace a more diffuse and extended molecular emission around the structure rather than its compact internal structure. This does not necessarily rule out a physical association to the feature, but it suggests that the correspondence is less robust than that seen for the PACS sources. However, if this source is associated with the Sagittarius Arm, it then challenges the interpretation of Davies et al. [7], who identify this feature as a bow shock, driven by DFK 49. A bow shock associated with a cluster member would be expected to reside at the cluster velocity, inconsistent with the partial Sagittarius Arm association found here.

The channel maps for the cluster velocity (Fig. 4.10 to 4.13) show gas emission in the region of IRAS 18364-0605 but without a clear spatial alignment. At $v = 102$ km/s, the gas contours broadly follow the shape of the source across all surveys, but manifest as fragmented emission rather than a coherent continuous envelope (right plot of Figure 5.2). This is therefore assumed to be emission that is more consistent with the source lying along the molecular barrier, rather than being physically embedded within a distinct molecular structure associated with the source itself. Furthermore, the fragmented rather than coherent emission at the cluster velocity is inconsistent with the continuous arc morphology expected from a bow shock structure. Despite weak evidence for association with the cluster, Table 4.2 reports high mean brightness temperatures over the velocity range, especially for the ^{12}CO transitions. This is presumably attributed to the contribution of the molecular barrier emission rather than the intrinsic emission from IRAS 18364-0605, which is also consistent with the interpretation established for PACS-A.

The molecular line ratios provide a final diagnostic, though the evidence here is less conclusive compared to PACS-A and PACS-B. At cluster velocity, $R_{(3-2)/(1-0)} = 0.479 \pm 0.004$ and $R_{12/13} = 4.778 \pm 0.065$, while for the Sagittarius Arm it is, $R_{(3-2)/(1-0)} = 0.643 \pm 0.012$ and $R_{12/13} = 6.059 \pm 0.274$. Although the $R_{(3-2)/(1-0)}$ ratio is higher at the Sagittarius arm velocity range, the difference is more modest than the difference found for PACS-A and PACS-B. This suggests that the excitation conditions at both velocities are more comparable for this source. The $R_{12/13}$ ratio is also marginally higher at the Sagittarius Arm velocity window, however, given the small differences in both ratios, the line ratio evidence alone is insufficient to conclusively assign IRAS 18364-0605 to either velocity component.

These results therefore suggest that the bow shock interpretation is unlikely, but because of the line of sight complexity towards this source, a definitive classification remains inconclusive. The elevated emission at the cluster velocity is most plausibly explained by the molecular barrier, although a physical association with the cluster environment is not fully excluded.

5.2.5 PACS-C and PACS-D

PACS-C and PACS-D are two unmapped far-infrared structures identified in the PACS160 image that are not clearly recovered in the RGB image. The fact these features appear only in the far-infrared regime that traces the coldest dust and not in the RGB, which traces warmer dust (in comparison to the cold dust), appears contradictory. However, the outlines of both structures are faintly discernible in the RGB image upon close inspection, suggesting that they are not entirely absent at shorter wavelength but rather too faint to be prominently recovered.

In Fig. 4.9, the highest integrated gas emission does not coincide with the molecular barrier, but rather with PACS-C. In the COHRS ^{12}CO(3-2) panel in particular, the blue contour lines cleanly trace the boundary of this structure (see left panel in Fig 5.3). This feature is, in fact, also detected in the integrated velocity maps in Fig. 4.8, where strong emission is seen in the upper right corner. Given its strong detection in both the PACS160 image and the CO emission maps, PACS-C most likely represents a deeply embedded cold molecular cloud. The emission from PACS-D is weaker than that of PACS-C, but is still detected. In Fig. 4.9, the COHRS ^{12}CO(3-2) panel shows a small compact contour at the center of the structure which is also displayed in the first plot of Fig. 5.3.

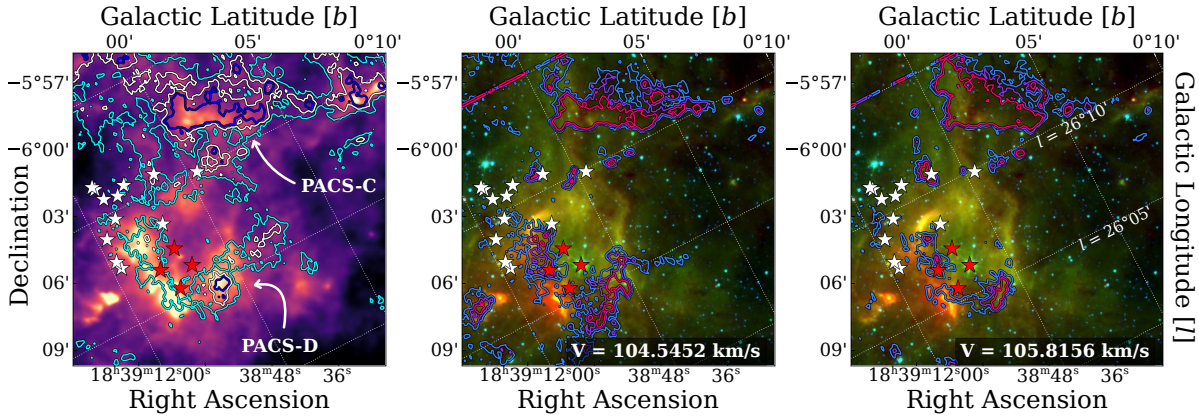


Fig. 5.3: Three plots centered on PACS-C and PACS-D with data from COHRS ^{12}CO(3-2) as contours. The first plot displays the moment 0 map over the cluster velocity ($90 - 115$ km/s) as contours with the levels, 10 (cyan), 20 (white), and 30 (blue) K km/s overlaid on the PACS160 dust emission image. The other two plots show the channel maps as contours overlaid on the RGB image at $v = 104.5$ and $v = 105.8$ km/s, with the levels at, 5 K (blue), 6.5 K (purple) and 8 K (magenta).

The channel maps further reveal the kinematic structure of PACS-C, which is clearly resolved across the velocity ranges from 103.3 to 107.1 km/s, with trailing emission persisting into the final channels in some surveys. This sequence reveals how this cold structure physically branches away from the primary molecular barrier. As the main barrier begins to dissipate and fade with increasing velocity, PACS-C systematically brightens and reaches its maximum intensity. PACS-D follows a similar but somewhat different pattern, first appearing at $v = 102$ km/s alongside the molecular barrier, although it appears to persist slightly beyond the barrier's dissipation. This is most clearly seen in the ^{12}CO surveys, where the central region of PACS-D shows emission between 104.5 to 107 km/s. The ^{13}CO surveys do not detect significant emission in the PACS-D region beyond $v = 105.8$ km/s, suggesting that PACS-D might be a less dense structure than PACS-C. The two channel maps in Fig. 5.3 show two velocity slices where both PACS-C and PACS-D can be distinguished.

5.3 The Molecular Gas Barrier and The South-West Region

The southwest region was first proposed as a distinct cluster by Deguchi et al. (2010) who suggested that a group of sources located too far away from the cluster core must belong to a separate cluster [8]. While their data were insufficient to conclusively support this claim, the results presented here provide new evidence that may strengthen this hypothesis.

Already in the PACS160 image, cold dust emission is clearly detected around the SW region, tracing a barrier that separates it from the cluster core. This is further strengthened by the molecular gas barrier identified in Fig. 4.8 which is consistently reproduced across both the optically thick ^{12}CO line and ^{13}CO line that traces the dense gas. The detection in both tracers implies a substantial molecular column density. In addition to its high column density, the barrier also acts as a physical boundary separating the cluster core and the SW region, further supporting the hypothesis that the SW is a separate cluster within the broader RSGC2 environment. The barrier is also seen to form a diagonal lane that extends along the direction of the galactic plane. The low intensity emission holes surrounding both regions additionally suggests that the RSGs or their progenitors have actively cleared molecular gas from their immediate environments, providing potential evidence of localized stellar feedback.

The wide-field moment 0 maps in Fig. 4.9 extended beyond the cluster core to reveal a broader geometry of the molecular gas surrounding RSGC2. Comparing these wide-field contours with the core cluster maps (Fig. 4.8) shows that the molecular barrier does not merely form a diagonal lane with a curl around the base of the SW region. Rather, it actively arcs around and encircles the SW stellar population. The spatial correspondence between the ^{12}CO and ^{13}CO gas contours traces the 160 µm far infrared dust emission around the SW region, providing strong evidence that this is a dense structure.

The three-dimensional structure of this molecular barrier is further revealed by the velocity segmented channel maps (Fig. 4.10 through 4.13). They refine the structural geometry initially inferred from the two-dimensional moment 0 projections. At $v = 102$ km/s, the channel map resolves the apparent encirclement of the SW region seen in the integrated maps as a projection effect caused by integrating across a wide velocity range. Across the initial ∼four velocity channels, an independent molecular structure extends from the eastern edge of the SW region up toward the northern cluster boundary. When integrated into a singular moment 0 map, these velocity dependent components blend together, mimicking a unified, encircling loop. The channel maps successfully resolve this ambiguity and the spatial distribution of molecular gas around the SW region becomes clear.

The spectral profiles provide additional and independent evidence that the sources in the SW behave slightly different from the core sources. In Fig. 4.1, the SW sources show both a broader peak and a higher line intensity for the cluster velocity window, which may indicate that the two regions represent two distinct clusters. At the very least, the SW could be a physical sub-cluster within the broader RSGC2 environment. A notable outlier in this picture is DFK 23, which exhibits broad spectral profiles and high line intensities characteristics of the SW, despite not being located in SW region. No alternative sub-cluster membership has been proposed to DFK 23 and its behavior may instead reflect that it is embedded within some local dense gas cloud. This interpretation is however not directly supported by the moment 0 maps nor the channel maps, which do not reveal any distinct structure associated with DFK 23.

Other than observing the spectral profile, the mean brightness temperatures in Table 4.1 provide further quantitative support for this interpretation. From the table, the sources with generally higher values are DFK 5, 10, 13, 23 and 68, all of which are located in close proximity to the barrier (see their positions in Fig. 1.2). On the other hand, the sources with the lowest mean temperatures are DFK 3, 52 and 14, all of which are located toward the center of the cluster core, away from the barrier.

5.4 CO line Ratios

The mean ratio for $R_{(3-2)/(1-0)}$, computed over the cluster velocity window ($90 - 115$ km/s) is consistent with the values reported for Galactic massive clusters [33]. This agreement suggests that the molecular gas conditions in the RSGC2 environment are broadly typical of massive stellar clusters, which is expected. The value that is reported over the whole spectral range ($-35 - 125$ km/s) decreases to $R_{(3-2)/(1-0)} = 0.389 \pm 0.004$, which is close to the value ($R_{(3-2)/(1-0)} = 0.35$) found by Park et al. [25]. The slightly elevated ratio toward RSGC2 compared to the broader Galactic average is consistent with the presence of a massive stellar cluster driving additional heating and excitation of the surrounding molecular gas.

Furthermore, the fact that the ratio calculated here is higher than the recorded value found by found by Park et al. [25] is also expected. The ratio reported by Park et al. [25] is averaged over a large area of the Galactic plane, which includes the diffuse gas in between the sources. This diffuse gas is cooler and less excited, and would lower the average ratio across the region. In contrast, the ratio computed here is averaged over only the sources, which excludes the cooler diffuse gas in between, making it reasonable for the ratio value to be slightly higher.

5.5 Future Work

Several important concepts have been discussed in this thesis and many more remain to be explored. One aspect is to continue investigating the spatial correspondence between the molecular gas and dust emission using the AstroHog [34] tool. By applying Histogram of oriented gradients (Hog) method, the degree of spatial alignment between the tracers can be measured, providing a more rigorous and quantitative evidence for or against the physical associations discovered here.

One of the central results in this thesis is the molecular gas barrier. The current analysis focuses on the structural and kinematic properties in the molecular gas. Future work should therefore aim to derive the physical properties of these structures, including gas temperature, molecular gas masses and dust masses. These measurements would place quantitative constraints on the nature of the barrier and its role in the evolution of the RSGC2. Similarly, the evidence for the SW region being a separate cluster is based on kinematic and structural analyses. This

hypothesis could be further tested by studying the individual stellar members of each region. By comparing radial velocities (similar to what Davies et al. [7] did) and their stellar ages between the sources in the SW to the core, could reveal differences which would be consistent with separate formation events.

Another research area is the infrared sources that are identified in this study. Several of them need further investigation, such as PACS-C and PACS-D. High resolution observations with ALMA or James Webb Space Telescope (JWST) would help determine the nature of these two structures. It would also be interesting to continue the analysis of IRAS 18364-0605 and resolve the ambiguity between the Sagittarius Arm and the cluster velocity associations.

Finally, the ALMA data cubes available for this study offer significant potential for further analysis beyond what was presented here. While a lot of data analysis was done on the ALMA cubes (See GitHub), not many of their results were included in this thesis. A more detailed analysis of these cubes could reveal important information about the physical conditions of the molecular gas immediately surrounding individual cluster members. However, it is important to note that due to spatial filtering, the ALMA observations are insensitive to large-scale ISM emission, meaning that such analysis would primarily probe the compact gas structures in the immediate vicinity of each source rather than the broader cluster environment. Additionally, mapping higher CO rotational transitions would better constrain the temperature and density of the molecular gas in the RSGC2 environments, continuing on the line ratio presented here.

6

Conclusion

This thesis has presented a multi-wavelength analysis of molecular gas and dust environments surrounding the Red Supergiant cluster RSGC2, combining large-scale public surveys (GRS, FUGIN, COHRS, GLIMPSE and Herschel/PACS) with high resolution ALMA observations. The large-scale spectral and spatial analysis successfully isolates distinct Galactic spiral arm crossings along the line of sight across a velocity window of -35-115 km/s. The molecular gas structures detected at the Sagittarius Arm velocity show strong spatial and kinematic correspondence with PACS-A and PACS-B, supporting their physical association with the Sagittarius Arm. The interpretation of IRAS 18364-0605 as a bow shock driven by DFK 49 is challenged by its partial Sagittarius Arm association, combined with the fragmented molecular emission at the cluster velocity, although a definitive classification remains inconclusive due to line-of-sight complexity. The supernova remnant candidate IRAS 18369-0557 is unambiguously detected at the cluster velocity, suggesting its progenitor star was physically associated with RSGC2. IRAS 18367-0556 shows a warm dust dominated emission profile and a lack of associated molecular gas emission, consistent with the interpretation of a highly reddened evolved massive star embedded within a warm circumstellar envelope. Two cold far-infrared structures, PACS-C and PACS-D, are identified with no clear RGB counterparts, suggesting they represent deeply embedded cold molecular structures that warrant further investigation.

At the cluster velocity, a dense molecular gas barrier is identified at $v = 102$ km/s which physically separates the primary cluster core from the SW region. The SW region shows distinct spectral and kinematic properties compared to the cluster core, including broader spectral profiles at the cluster velocities, higher line intensities, and a physical molecular gas boundary. Combined with the original suggestion of Deguchi et al. (2010), these results support the hypothesis that the SW might be a separate sub-cluster. Additionally, low-intensity emission holes surrounding individual cluster members provide clear evidence of localized stellar feedback, consistent with RSGs actively clearing molecular gas from their immediate environments in a manner expected for a young massive cluster in the gas expulsion phase of its evolution.

Finally, the mean $R_{(3-2)/(1-0)}$ value over the cluster velocity window is consistent with values reported for Galactic massive clusters, confirming that the molecular gas conditions in RSGC2 are broadly typical of such environments. While the low value of $R_{12/13}$ suggests that the ^{12}CO emission towards the DFK sources are highly optically thick.

Together, these results provide new insights into the multi-phase ISM environment of RSGC2, revealing a complex interplay between stellar feedback, molecular gas dynamics, and large-scale Galactic structures. The identification of a molecular barrier separating a possible SW sub-cluster, combined with evidence of active gas clearing by RSGs, places RSGC2 in the context of an actively evolving young massive cluster in the gas expulsion phase of its evolution.

Bibliography

[1] H. J. Lamers and E. M. Levesque, *Understanding Stellar Evolution* (2514-3433). IOP Publishing, 2017. DOI: 10.1088/978-0-7503-1278-3.

[2] ESO. "Hertzsprung-russell diagram," Www.eso.org. [Online]. Available: https://www.eso.org/public/sweden/images/eso0728c/?lang.

[3] E. M. Levesque, *Astrophysics of Red Supergiants* (2514-3433). IOP Publishing, 2017. DOI: 10.1088/978-0-7503-1329-2.

[4] A. R. Choudhuri, *Astrophysics for Physicists*. Cambridge University Press, Mar. 2010. DOI: 10.1017/cbo9780511802218.

[5] S. F. P. Zwart, S. L. W. McMillan, and M. Gieles, "Young massive star clusters," *Annual Review of Astronomy and Astrophysics*, vol. 48, pp. 431–493, Sep. 2010. DOI: 10.1146/annurev-astro-081309-130834.

[6] I. Negueruela et al., "Red supergiants around the obscured open cluster stephenson2," *Astronomy & Astrophysics*, vol. 547, A15, Oct. 2012. DOI: 10.1051/0004-6361/201219540.

[7] B. Davies, D. F. Figer, R.-P. Kudritzki, J. MacKenty, F. Najarro, and A. Herrero, "A massive cluster of red supergiants at the base of the scutum-crux arm," *The Astrophysical Journal*, vol. 671, pp. 781–801, 2007. DOI: 10.1086/522224.

[8] S. Deguchi, J.-i. Nakashima, Y. Zhang, S. S. N. Chong, K. Koike, and S. Kwok, "Sio and h2o maser observations of red supergiants in star clusters embedded in the galactic disk," *Publications of the Astronomical Society of Japan*, vol. 62, no. 2, pp. 391–407, Apr. 2010. DOI: 10.1093/pasj/62.2.391.

[9] "Introduction to the iras," NASA/IPAC. [Online]. Available: https://irsa.ipac.caltech.edu/IRASdocs/iras.html.

[10] P. Hodge, *Milky way galaxy | size, definition, & facts | britannica*, Encyclopædia Britannica, 2020.

[11] M. J. Reid et al., "Trigonometric parallaxes of high-mass star-forming regions: Our view of the milky way," *The Astrophysical Journal*, vol. 885, p. 131, Nov. 2019. DOI: 10.3847/1538-4357/ab4a11.

[12] M. J. Reid, T. M. Dame, K. M. Menten, and A. Brunthaler, "A parallax-based distance estimator for spiral arm sources," *The Astrophysical Journal*, vol. 823, p. 77, May 2016. DOI: 10.3847/0004-637x/823/2/77.

[13] B. T. Draine, *Physics of the Interstellar and Intergalactic Medium*. Princeton University Press, 2011.

[14] A. D. Bolatto, M. Wolfire, and A. K. Leroy, "The co-to-h2 conversion factor," *Annual Review of Astronomy and Astrophysics*, vol. 51, no. 1, pp. 207–268, Aug. 2013. DOI: 10.1146/annurev-astro-082812-140944.

[15] T. L. Wilson, K. Rohlfs, and S. Hüttemeister, *Tools of Radio Astronomy*. Springer Berlin Heidelberg, 2013. DOI: 10.1007/978-3-642-39950-3.

[16] T. L. Wilson, "Abundances in the interstellar medium," *The Astronomy and Astrophysics Review*, vol. 4, no. 1, pp. 1–33, Mar. 1992. DOI: 10.1007/BF00873568.

[17] NASA/IPAC, *Near, mid and far-infrared*, https://www.ipac.caltech.edu/page/near-mid-far-infrared, 2020.

[18] J. J. Condon and S. M. Ransom, *Essential Radio Astronomy*. ADS, 2016.

[19] "Flux density," NRAO Science Site. [Online]. Available: https://science.nrao.edu/facilities/vla/proposing/TBconv.

[20] Astropy Collaboration et al., "The Astropy Project: Sustaining and Growing a Community-oriented Open-source Project and the Latest Major Release (v5.0) of the Core Package," *apj*, vol. 935, no. 2, p. 167, Aug. 2022, Art. no. 167. DOI: 10.3847/1538-4357/ac7c74. arXiv: 2206.14220 [astro-ph.IM].

[21] A. Ginsburg, T. Robitaille, C. Beaumont, C. Leroy, E. Rosolowsky, and E. Koch, *Spectral cube documentation*, SpectraCube.

[22] "Alma - atacama large millimeter/submillimeter array," www.eso.org. [Online]. Available: https://www.eso.org/public/teles-instr/alma/.

[23] J. M. Jackson et al., "The boston university-five college radio astronomy observatory galactic ring survey," *The Astrophysical Journal Supplement Series*, vol. 163, no. 1, pp. 145–159, Mar. 2006. DOI: 10.1086/500091.

[24] T. Umemoto et al., "Forest unbiased galactic plane imaging survey with the nobeyama 45 m telescope (fugin). i. project overview and initial results," *Publications of the Astronomical Society of Japan*, vol. 69, no. 5, p. 78, Oct. 2017. DOI: 10.1093/pasj/psx061.

[25] G. Park et al., "12co (3–2) high-resolution survey (cohrs) of the galactic plane: Complete data release," *The Astrophysical Journal Supplement Series*, vol. 264, no. 1, p. 16, Dec. 29, 2022. DOI: 10.3847/1538-4365/ac9b59.

[26] E. Churchwell et al., "The spitzer/glimpse surveys: A new view of the milky way," *Publications of the Astronomical Society of the Pacific*, vol. 121, no. 877, p. 213, Mar. 12, 2009. DOI: 10.1086/597811.

[27] S. Molinari et al., "Hi-gal, the herschel infrared galactic plane survey: Photometric maps and compact source catalogues," *Astronomy & Astrophysics*, vol. 591, A149, Jul. 4, 2016. DOI: 10.1051/0004-6361/201526380.

[28] A. Poglitsch et al., "The photodetector array camera and spectrometer (pacs) on the herschel space observatory," *Astronomy & Astrophysics*, vol. 518, p. L2, Jul. 16, 2010. DOI: 10.1051/0004-6361/201014535.

[29] T. M. Dame, D. Hartmann, and P. Thaddeus, "The milky way in molecular clouds: A new complete co survey," *The Astrophysical Journal*, vol. 547, no. 2, pp. 792–813, Feb. 2001. DOI: 10.1086/318388.

[30] C. A. Beichman, G. Neugebauer, H. J. Habing, P. E. Clegg, and T. J. Chester, "Infrared astronomical satellite (iras) catalogs and atlases.volume 1: Explanatory supplement.," *Infrared astronomical satellite (IRAS) catalogs and atlases. Volume 1: Explanatory supplement*, vol. 1, 1988.

[31] J. R. Taylor, *An introduction to error analysis: the study of uncertainties in physical measurements*. MIT Press, 2022.

[32] A. Ginsburg et al., *Moment maps and statistics*, SpectraCube.

[33] C. H. Peñaloza, P. C. Clark, S. C. Glover, and R. S. Klessen, "Co line ratios in molecular clouds: The impact of environment," *Monthly Notices of the Royal Astronomical Society*, vol. 475, no. 2, pp. 1508–1520, 2018.

[34] J. D. Soler et al., "Histogram of oriented gradients: A technique for the study of molecular cloud formation," *Astronomy & Astrophysics*, vol. 622, A166, Feb. 2019. DOI: 10.1051/0004-6361/201834300.

A

Appendix

A.1 ALMA spectral profile

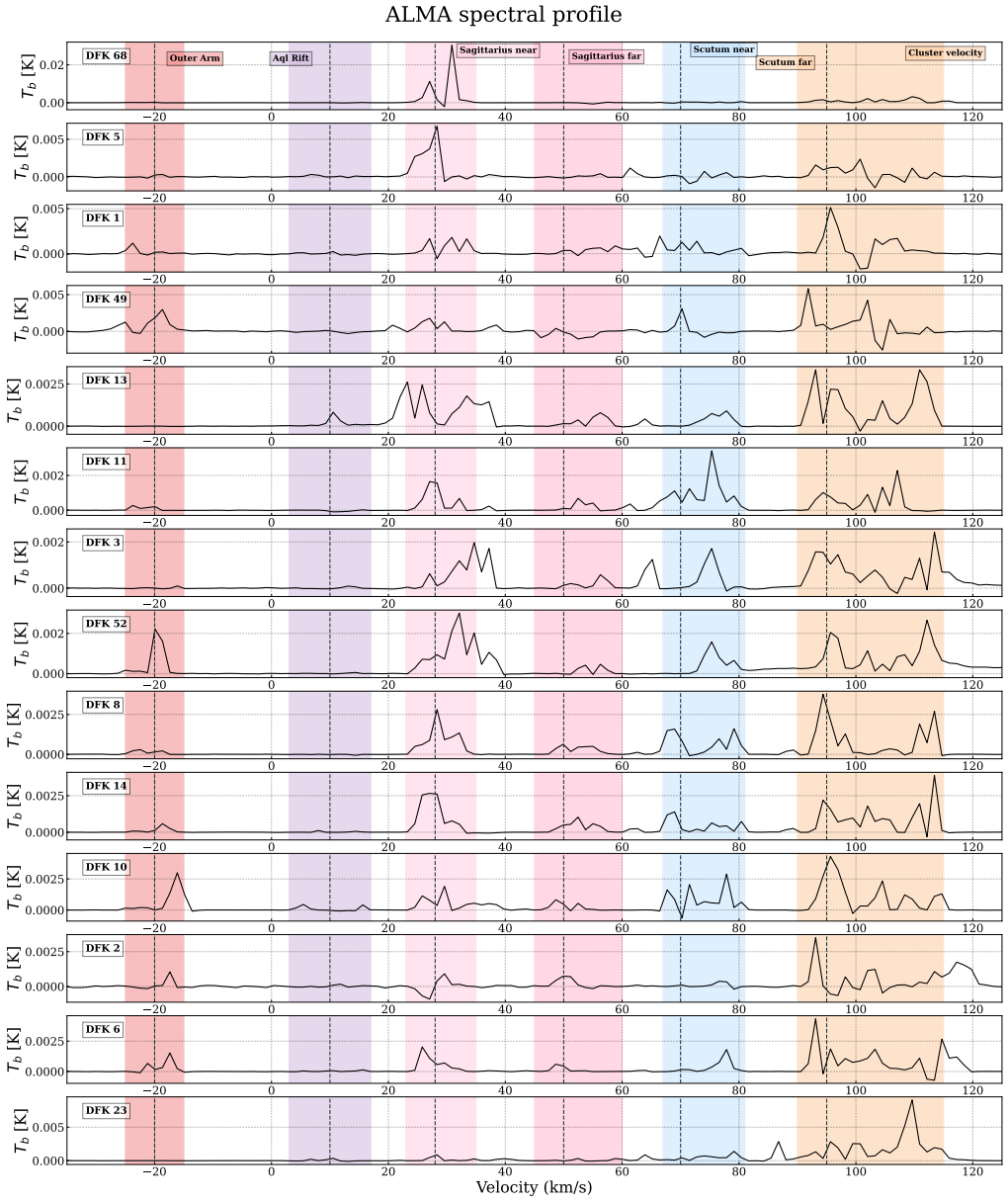


Fig. A.1: The spectral profile of the ALMA ^{12}CO(2-1) survey.

A.2 Average Brightness Temperature Over the Spectral Range

Table A.1: Average brightness temperatures over the velocity range of -35 km/s to 125 km/s for each survey with top 5 DFK sources highlighted. Note that the unit for all averages are in Kelvin.

DFK	**FUGIN** ^{12}CO(1-0)	**COHRS** ^{12}CO(3-2)	**GRS** ^{13}CO(1-0)	**FUGIN** ^{13}CO(1-0)	**ALMA** ^{12}CO(2-1)
1	1.790 ± 0.044	0.600 ± 0.016	0.330 ± 0.010	0.370 ± 0.018	$0.040 \pm 9 \cdot 10^{-4}$
2	1.260 ± 0.022	0.410 ± 0.017	0.260 ± 0.009	0.260 ± 0.019	$0.020 \pm 5 \cdot 10^{-4}$
3	1.040 ± 0.029	0.390 ± 0.010	0.220 ± 0.010	0.240 ± 0.021	$0.040 \pm 1 \cdot 10^{-4}$
5	1.720 ± 0.026	0.750 ± 0.016	0.420 ± 0.008	0.340 ± 0.013	$0.040 \pm 4 \cdot 10^{-4}$
6	1.270 ± 0.039	0.440 ± 0.009	0.280 ± 0.005	0.260 ± 0.014	$0.050 \pm 2 \cdot 10^{-4}$
8	1.070 ± 0.033	0.460 ± 0.009	0.250 ± 0.015	0.280 ± 0.022	$0.050 \pm 2 \cdot 10^{-4}$
10	1.600 ± 0.041	0.670 ± 0.007	0.340 ± 0.008	0.390 ± 0.014	$0.070 \pm 1 \cdot 10^{-4}$
11	1.230 ± 0.049	0.480 ± 0.020	0.310 ± 0.009	0.320 ± 0.026	$0.040 \pm 1 \cdot 10^{-4}$
13	1.430 ± 0.013	0.580 ± 0.019	0.400 ± 0.009	0.370 ± 0.007	$0.070 \pm 1 \cdot 10^{-4}$
14	1.040 ± 0.026	0.450 ± 0.014	0.250 ± 0.015	0.260 ± 0.020	$0.060 \pm 1 \cdot 10^{-4}$
23	1.700 ± 0.034	0.580 ± 0.021	0.410 ± 0.011	0.370 ± 0.016	$0.080 \pm 1 \cdot 10^{-4}$
49	1.700 ± 0.044	0.610 ± 0.026	0.360 ± 0.010	0.300 ± 0.014	$0.040 \pm 6 \cdot 10^{-4}$
52	1.040 ± 0.057	0.390 ± 0.016	0.240 ± 0.011	0.310 ± 0.025	$0.060 \pm 1 \cdot 10^{-4}$
68	1.810 ± 0.079	0.860 ± 0.016	0.360 ± 0.012	0.390 ± 0.022	$0.090 \pm 1 \cdot 10^{-4}$

Table A.2: Average brightness temperatures over the velocity range of -35 km/s to 125 km/s for each survey. Note that the unit for all intensity averages are in Kelvin.

Source	**FUGIN** ^{12}CO(1-0)	**COHRS** ^{12}CO(3-2)	**GRS** ^{13}CO(1-0)	**FUGIN** ^{13}CO(1-0)
IRAS 18369-0557	1.123 ± 0.011	0.566 ± 0.007	0.320 ± 0.005	0.304 ± 0.009
IRAS 18367-0556	1.213 ± 0.019	0.464 ± 0.010	0.348 ± 0.007	0.290 ± 0.016
IRAS 18364-0605	1.709 ± 0.010	0.721 ± 0.006	0.366 ± 0.006	0.318 ± 0.005
PACS-A	1.740 ± 0.023	0.848 ± 0.010	0.397 ± 0.005	0.344 ± 0.010
PACS-B	1.225 ± 0.020	0.585 ± 0.009	0.282 ± 0.007	0.265 ± 0.006

A.3 Moment 0 map of the Outer Arm

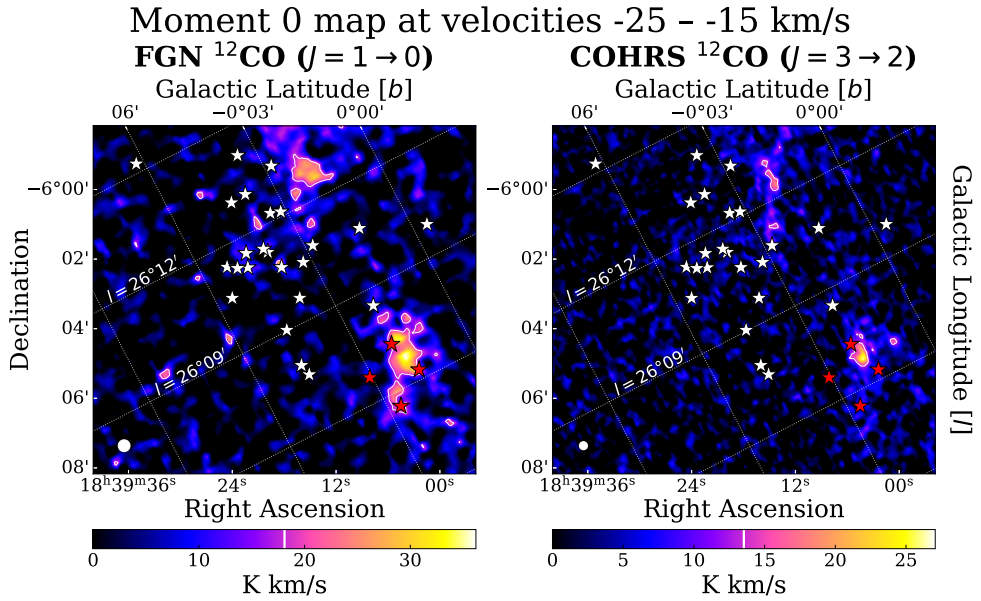


Fig. A.2: FUGIN ^{12}CO(1-0) and COHRS ^{12}CO(3-2) Moment 0 maps integrated over the Outer Arm velocity range. White and red stellar symbols mark the cluster core and the SW members, respectively.

A.4 More Channel maps over the Sagittarius Arm

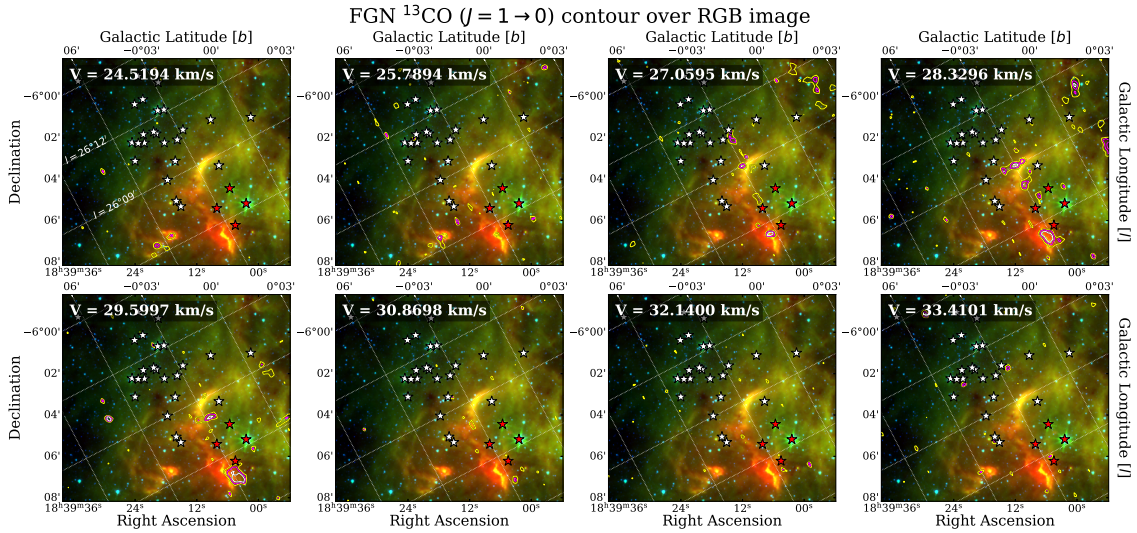


Fig. A.3: FUGIN ^{13}CO(1-0) velocity channel maps across the Sagittarius Arm, overlaid on an RGB image. The emission is represented by contours at temperature levels of 2.5 K (yellow), 3.5 K (magenta) and 4.5 K (white).

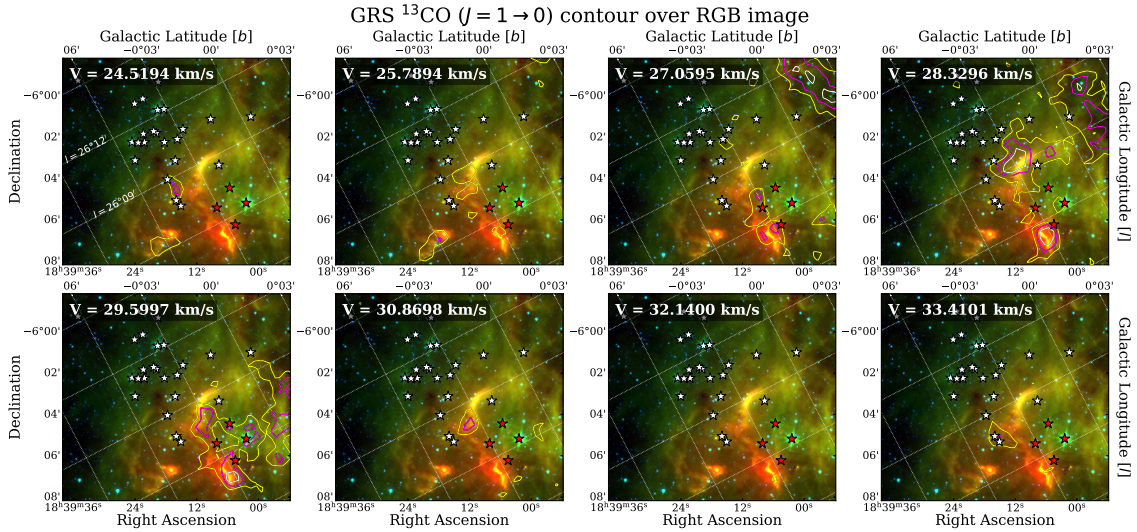


Fig. A.4: GRS ^{13}CO(1-0)velocity channel maps across the Sagittarius Arm, overlaid on an RGB image. The emission is represented by contours at temperature levels of 1 K (yellow), 1.5 K (magenta), 2 K (white).

A.5 Ratio for all sources

Table A.3: Line intensity ratios for the observed DFK sources over the velocity range of -35 km/s to 125 km/s. The overall sample average for $R_{(3-2)/(1-0)} = 0.389 \pm 0.004$, and for the isotopic ratio $R_{12/13} = 4.383 \pm 0.078$.

Source	$R_{(3-2)/(1-0)}$	$R_{12/13}$
1	0.338 ± 0.012	4.833 ± 0.266
2	0.325 ± 0.015	4.757 ± 0.358
3	0.371 ± 0.014	4.281 ± 0.387
5	0.434 ± 0.011	5.031 ± 0.202
6	0.344 ± 0.013	4.846 ± 0.302
8	0.432 ± 0.016	3.745 ± 0.309
10	0.421 ± 0.012	4.099 ± 0.181
11	0.393 ± 0.023	3.813 ± 0.349
13	0.406 ± 0.014	3.889 ± 0.086
14	0.430 ± 0.017	3.937 ± 0.307
23	0.344 ± 0.014	4.607 ± 0.215
49	0.358 ± 0.018	5.581 ± 0.302
52	0.371 ± 0.025	3.341 ± 0.319
68	0.474 ± 0.022	4.597 ± 0.327

Table A.4: Line intensity ratios for the IRAS and PACS sources over the spectral range (-35 to 125 km/s).

Sources	$R_{(3-2)/(1-0)}$	$R_{12/13}$
IRAS 18369-0557	0.504 ± 0.008	3.695 ± 0.111
IRAS 18367-0556	0.382 ± 0.010	4.176 ± 0.242
IRAS 18364-0605	0.422 ± 0.004	5.367 ± 0.095
PACS-A	0.487 ± 0.009	5.057 ± 0.155
PACS-B	0.477 ± 0.011	4.620 ± 0.133

A.6 ALMA survey

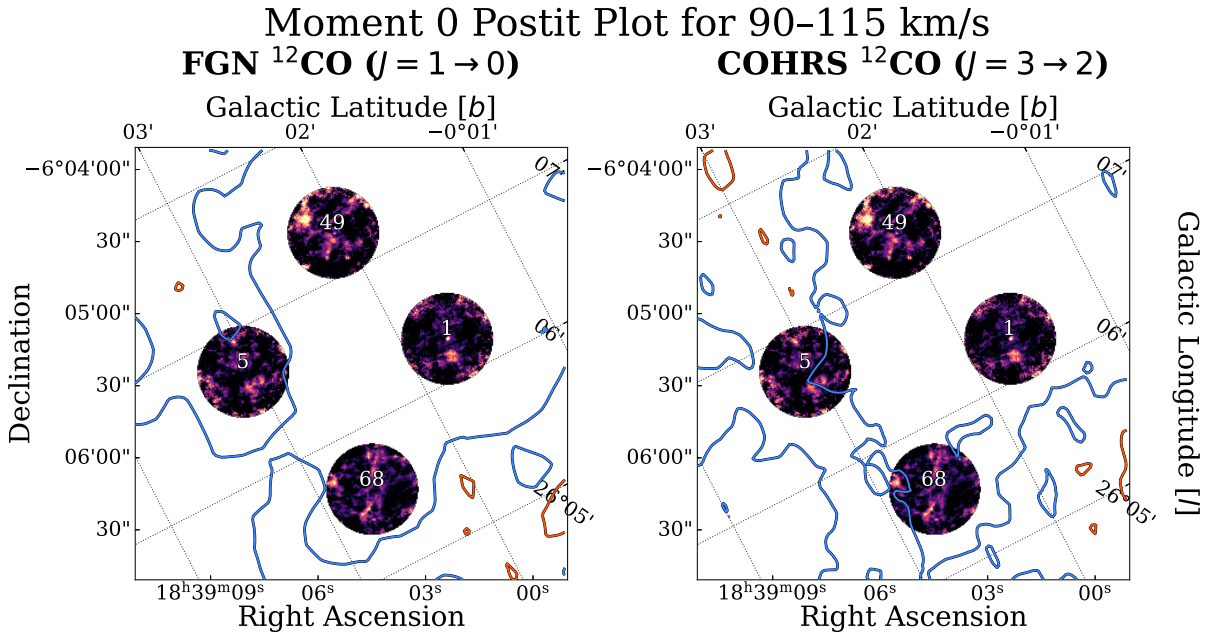


Fig. A.5: Moment 0 maps on the SW sources, using ALMA data. Overlaid is the Moment 0 contours from FUGIN ^{12}CO(1-0) and COHRS ^{12}CO(3-2).

DEPARTMENT OF PHYSICS AND ASTRONOMY
CHALMERS UNIVERSITY OF TECHNOLOGY
Gothenburg, Sweden
www.chalmers.se



CHALMERS
UNIVERSITY OF TECHNOLOGY